NASA Contractor Report 198535

Linear Instability of a Uni-Directional Transversely Sheared Mean Flow

David W. Wundrow
NYMA, Inc.
Brook Park, Ohio

October 1996

Prepared for
Lewis Research Center
Under Contract NAS3–27186

National Aeronautics and
Space Administration

Linear instability of a uni-directional transversely sheared mean flow

By DAVID W. WUNDROW
Nyma Inc., Lewis Research Center Group, Cleveland, Ohio 44135, USA

Abstract

The effect of spanwise-periodic mean-flow distortions (i.e. streamwise-vortex structures) on the evolution of small-amplitude, single-frequency instability waves in an otherwise two-dimensional shear flow is investigated. The streamwise-vortex structures are taken to be just weak enough so that the spatially growing instability waves behave (locally) like linear perturbations about a uni-directional transversely sheared mean flow. Numerical solutions are computed and discussed for both the mean flow and the instability waves. The influence of the streamwise-vortex wavelength on the properties of the most rapidly growing instability wave is also discussed.

1. Introduction

The effect streamwise-vortex structures have on the development of otherwise two-dimensional shear flows is of much interest for both theoretical and technological reasons. The theoretical interest stems from the role steady streamwise vortices play in amplifying three-dimensional disturbances in laminar shear flows. Transition to turbulence in relatively two-dimensional shear flows is virtually always preceded by the rapid growth of three-dimensional disturbances. The technological interest arises from the ability of steady streamwise-vortex structures to significantly enhance the mixing process. Mixing enhancement in shear flows has received renewed attention in recent years primarily due to the

current interest in supersonic combustion and noise reduction for the high-speed civil transport. The efficiency of scramjet propulsion systems depends on the time required to achieve a flammable (near-stoichiometric) mix of fuel and air within the combustor. Noise reduction in the mixer/ejector nozzle concept is accomplished by mixing entrained ambient air with high-speed exhaust plumes inside an acoustically treated ejector.

Steady streamwise-vortex structures can arise in laminar–turbulent transition experiments due to wall roughness, free-stream disturbances and/or imperfections in the relatively two-dimensional excitation devices. In technological applications, the vortex structures may be produced by surface geometry or three-dimensional devices such as ramp injectors, tabs, or trip wires. In either case, the resulting three-dimensional mean flow will usually have a primary-flow direction – provided, of course, the cross flow associated with the streamwise-vortex structure is not too strong. Since the mean velocity component in the primary-flow direction is much larger than the velocity components in the cross-flow plane, the mean flow is governed by a set of equations that become of nearly boundary-layer type in the high-Reynolds-number limit (Davis & Rubin 1980). Small-amplitude disturbances propagating on such flows will behave (at least locally) like linear perturbations about a uni-directional transversely sheared mean flow. This paper is an attempt to provide a systematic first principles analysis of the linear stability characteristics of such disturbances using a combination of numerical techniques and high-Reynolds-number asymptotic methods.

It is well known that steady streamwise-vortex structures can strongly influence the development of otherwise two-dimensional shear flows by amplifying three-dimensional disturbances through a kind of parametric-resonance or secondary-instability mechanism (Nayfeh 1981; Henningson 1987; Bennett & Hall 1988; Nayfeh & Al-Maaitah 1988; Hall & Seddougui

1989; and others). This phenomenon has most often been investigated in the context of the secondary instability of Görtler vortices on curved-wall boundary layers (e.g. Hall & Horseman 1991 and Li & Malik 1995). These investigations have been primarily concerned with determining the temporal amplification rates of the so-called fundamental secondary instabilities, i.e. the instabilities having a spanwise wavelength equal to that of the Görtler vortices. However, Li & Malik (1995) also investigated instabilities having spanwise wavelengths equal to twice that of the Görtler vortices and found that the temporal growth rates of these so-called subharmonic secondary instabilities can be comparable with the growth rates of the fundamental instabilities.

Goldstein & Wundrow (1995, hereafter referred to as GW) analyzed the effect of introducing a small-amplitude spanwise-periodic cross flow into a Blasius boundary layer. The imposed cross flow produces a distortion in the streamwise velocity component that initially grows with increasing downstream distance, reaches a maximum and then eventually decays through the action of viscosity. This decay occurs slowly and allows the distortion to destabilize the flow to three-dimensional inviscid disturbances over a relatively long streamwise distance. Goldstein & Wundrow concentrated on the limit where the spanwise wavelength of the mean-flow distortion is large compared to the boundary-layer thickness. This long-wavelength limit allows analytic solutions to be obtained for both the steady and unsteady components of the flow and therefore elucidates the relevant physical mechanisms. The authors also solved the spatial stability problem rather than the temporal one since it is the spatial theory that correctly describes convectively unstable flows. They found that the most amplified instability has a spanwise wavelength equal to twice that of the mean-flow distortion (i.e. it is a subharmonic secondary instability) and, furthermore, that the fundamental

secondary instability remains damped in the long-wavelength limit.

The primary objective of the present paper is to extend the linear stability analysis of GW to the case where the spanwise wavelength of the mean-flow distortion is of the same order of magnitude as the shear-layer thickness. The linear stability analysis will also be generalized to spatially growing disturbances having an arbitrary, bounded behavior in the spanwise direction. This will enable an investigation of the effect of streamwise-vortex wavelength on the spatial growth rate and spanwise wavelength of the most rapidly growing secondary instability. The results of such an investigation should be of much technological interest since they could help guide the development of more efficient mixing-enhancement techniques. In order to carry out the investigation, numerical schemes must be developed for computing the evolution of the steady three-dimensional base flow as well as for determining the linear stability characteristics of a general time-periodic perturbation. These numerical schemes will also permit an evaluation of the follow-on nonlinear stage in the development of the most amplified instability wave analyzed in Wundrow & Goldstein (1994).

The paper is organized as follows. In §2, governing equations for the steady base flow and the linear unsteady perturbation are derived in the high-Reynolds-number limit. The numerical schemes used to solve these equations are described in §§3 and 4. In §5, a comparison of the results predicted by the long-wavelength solution developed in GW (and extended in appendix B) to those determined by a numerical solution to the aforementioned governing equations is presented. Numerical results for an order-one spanwise wavelength solution are also presented and discussed in §5.

2. Formulation

Attention is focused on an incompressible shear flow formed at the interface between two parallel streams of differing velocity or, alternatively, between a single parallel stream and a flat plate. The Cartesian coordinate system (x, y, z) is attached to the interface with x in the direction of the external flow, y normal to the interface, and z in the spanwise direction. The origin of the coordinate system is located a distance L_* downstream of the initial point of contact between the upper and lower streams or between the upper stream and the plate. All lengths are non-dimensionalized by δ_* where δ_* characterizes the local shear-layer thickness at $x = 0$. The $*$ subscript is used to indicate dimensional quantities. The time t, velocity $\boldsymbol{u} = \boldsymbol{i}u + \boldsymbol{j}v + \boldsymbol{k}w$, and pressure p are non-dimensionalized by δ_*/U_*, U_* and $\rho_* U_*^2$, respectively, where U_* characterizes the velocity of the external flow and ρ_* is the density. With this non-dimensionalization, the Navier–Stokes equations become

$$\boldsymbol{u}_t + \boldsymbol{u}\cdot\boldsymbol{\nabla}\boldsymbol{u} + \boldsymbol{\nabla}p = R^{-1}\boldsymbol{\nabla}^2\boldsymbol{u}, \tag{2.1}$$

$$\boldsymbol{\nabla}\cdot\boldsymbol{u} = 0, \tag{2.2}$$

where $\boldsymbol{\nabla} \equiv \boldsymbol{i}\partial/\partial x + \boldsymbol{j}\partial/\partial y + \boldsymbol{k}\partial/\partial z$ is the gradient operator,

$$R \equiv \delta_* U_*/\nu_* \gg 1 \tag{2.3}$$

is the local Reynolds number, ν_* is the kinematic viscosity and an independent variable used as a subscript denotes differentiation with respect to that variable.

The solutions to (2.1) and (2.2) of interest here are expressed as the sum of a steady base flow and a time-dependent perturbation,

$$\boldsymbol{u} = \boldsymbol{U}(\boldsymbol{x}) + \epsilon\acute{\boldsymbol{u}}(\boldsymbol{x}, t), \tag{2.4}$$

$$p = P(\boldsymbol{x}) + \epsilon \acute{p}(\boldsymbol{x}, t), \tag{2.5}$$

where $\epsilon \ll 1$ characterizes the local amplitude of the perturbation at $x = 0$. The steady, spanwise-periodic, base flow $\{\boldsymbol{U}, P\}$ evolves over the long streamwise scale,

$$x_2 \equiv x/R, \tag{2.6}$$

and expands like

$$\boldsymbol{U} = i\boldsymbol{U}_0(x_2, y, z) + R^{-1}\boldsymbol{V}_0(x_2, y, z) + \cdots, \tag{2.7}$$

$$P = P_e(x_2) + \cdots + R^{-2}P_0(x_2, y, z) + \cdots, \tag{2.8}$$

for order one x_2, y and z as $R \to \infty$, where $\boldsymbol{V}$ denotes the base-flow velocity in the transverse (or y–z) plane, P_e denotes the pressure imposed on the shear layer by the external inviscid flow and P_0 is the first term in the pressure expansion to have a transverse variation. The unsteady flow $\{\acute{\boldsymbol{u}}, \acute{p}\}$ also evolves on the x_2 scale, starting as a linear perturbation and becoming nonlinear sufficiently far downstream (for details see Wundrow & Goldstein 1994). However, the present analysis only considers the local linear solution (i.e. the linear solution valid over streamwise distances of order δ_*) so $\{\acute{\boldsymbol{u}}, \acute{p}\}$ are expressed as

$$\acute{\boldsymbol{u}} = \mathrm{Re}\left[\hat{\boldsymbol{u}}(y, z)\mathrm{e}^{\mathrm{i}X}\right] + \cdots, \tag{2.9}$$

$$\acute{p} = \mathrm{Re}\left[\hat{p}(y, z)\mathrm{e}^{\mathrm{i}X}\right] + \cdots, \tag{2.10}$$

for order one x, y, z and t, where

$$X \equiv R\int \alpha(x_2)\mathrm{d}x_2 - St, \tag{2.11}$$

α is the local streamwise wavenumber, $S \equiv \delta_* F_*/U_*$ is the local Strouhal number (or non-dimensional angular frequency) and the dots indicate higher-order terms in ϵ as well as R^{-1}.

It was shown in GW that the leading-order base-flow solution is determined by the so-called boundary-region equations,

$$U_0 U_{0x_2} + \boldsymbol{V}_0 \cdot \boldsymbol{\nabla}_T U_0 + P_e' = \nabla_T^2 U_0, \tag{2.12}$$

$$U_0 \boldsymbol{V}_{0x_2} + \boldsymbol{V}_0 \cdot \boldsymbol{\nabla}_T \boldsymbol{V}_0 + \boldsymbol{\nabla}_T P_0 = \nabla_T^2 \boldsymbol{V}_0, \tag{2.13}$$

$$U_{0x_2} + \boldsymbol{\nabla}_T \cdot \boldsymbol{V}_0 = 0, \tag{2.14}$$

(Davis & Rubin 1980) where $\boldsymbol{\nabla}_T \equiv \boldsymbol{j}\partial/\partial y + \boldsymbol{k}\partial/\partial z$ is the gradient operator in the transverse plane and a prime denotes differentiation with respect to the argument. The pressure fluctuation associated with the local instability wave was shown in GW to satisfy a generalized Rayleigh stability equation

$$\boldsymbol{\nabla}_T \cdot \left[\frac{\boldsymbol{\nabla}_T \hat{p}}{(U_0 - c)^2} \right] - \frac{\alpha^2 \hat{p}}{(U_0 - c)^2} = 0, \tag{2.15}$$

where $c \equiv S/\alpha$ is the local phase speed.

Equations (2.12)–(2.15) must be solved subject to

$$\left.\begin{aligned} \{U_0,\ \boldsymbol{V}_0,\ \hat{p}_y\} &= 0 \qquad \text{at} \quad y = 0 \\ \{U_0,\ \boldsymbol{V}_0,\ \hat{p}\} &\to \{U_e,\ \boldsymbol{j}V_0^{(+)},\ 0\} \ \text{ as } \ y \to +\infty \end{aligned}\right\}, \tag{2.16}$$

for wall-bounded flows, or

$$\{U_0,\ \boldsymbol{V}_0,\ \hat{p}\} \to \{(U_e^2 \pm 1)^{1/2},\ \boldsymbol{j}V_0^{(\pm)},\ 0\} \quad \text{as} \quad y \to \pm\infty, \tag{2.17}$$

for unbounded flows, where $U_e(x_2)$ satisfies

$$U_e U_e' = -P_e', \tag{2.18}$$

and $V_0^{(+)}$ and $V_0^{(-)}$ denote the scaled normal velocity components induced by the displacement thickness at the upper and lower edges of the shear layer, respectively. It will be

assumed that the spanwise varying part of the base flow remains confined to the shear layer. The external inviscid flow then remains two-dimensional to the required level of approximation and the functions $V_0^{(\pm)}(x_2, y)$ are determined as part of the solution to (2.12)–(2.14).

In addition to the normal-boundary conditions given by (2.16) or (2.17), (2.12)–(2.15) must be solved subject to boundary conditions in the spanwise direction. The steady base flow is required to be periodic in the spanwise direction with period $2\pi/\beta$. The spanwise-boundary condition for the unsteady perturbation is somewhat more general in that $\hat{p}$ need only remain bounded as $z \to \pm\infty$.

3. Steady base flow

The steady base flow is computed with a method similar to that used by Rubin, Khosla & Saari (1977) to analyze laminar flow in rectangular channels. The transversely varying component of the pressure is eliminated from the problem by applying the operator $\boldsymbol{\nabla}_T\times$ to (2.13). This leads to

$$U_0 U_{0x_2} + \boldsymbol{V}_0\cdot\boldsymbol{\nabla}_T U_0 + P_e' = \nabla_T^2 U_0, \tag{3.1}$$

$$U_0 \Omega_{0x_2} + \boldsymbol{V}_0\cdot\boldsymbol{\nabla}_T \Omega_0 - U_{0x_2}\Omega_0 - V_{0x_2}U_{0z} + W_{0x_2}U_{0y} = \nabla_T^2 \Omega_0, \tag{3.2}$$

$$\Omega_0 = W_{0y} - V_{0z}, \tag{3.3}$$

$$U_{0x_2} + \boldsymbol{\nabla}_T\cdot\boldsymbol{V}_0 = 0, \tag{3.4}$$

where Ω_0 is the leading-order term in the large-R expansion of the streamwise component of vorticity. In view of (2.16), (2.17) and the requirement that the spanwise varying part of

the base flow remain confined to the shear layer, (3.1)–(3.4) must be solved subject to

$$\left.\begin{aligned} \{U_0,\ V_0,\ W_0,\ \Omega_0 - W_{0y}\} &= 0 \qquad \text{at} \quad y = 0 \\ \{U_0,\ V_0,\ W_{0y},\ \Omega_0\} &\to \{U_e,\ V_0^{(+)},\ 0,\ 0\} \quad \text{as} \quad y \to +\infty \end{aligned}\right\}, \tag{3.5}$$

for wall-bounded flows,

$$\{U_0,\ V_0,\ W_{0y},\ \Omega_0\} \to \{(U_e^2 \pm 1)^{1/2},\ V_0^{(\pm)},\ 0,\ 0\} \quad \text{as} \quad y \to \pm\infty, \tag{3.6}$$

for unbounded flows, and, in either case, the solution must be periodic in z with period $2\pi/\beta$.

In order to provide sufficient numerical resolution, the physical plane (x_2, y, z) is mapped into a computational plane (ξ, η, ζ) using the coordinate transformations

$$x_2 = \xi - \xi^0, \quad y = \theta(\xi)g(\eta) + \psi(\xi), \quad z = \beta^{-1}\zeta \tag{3.7}$$

where $\xi^0 \equiv L_*/R\delta_*$ is the scaled distance to the virtual origin of the shear flow, $\theta \equiv \sqrt{\xi/U_e}$ accounts for viscous spreading, g is used to concentrate grid points near the dividing stream surface and ψ allows for an arbitrary displacement of that surface. The specific forms of g and ψ used in the computations are given in §5. For now, it suffices to note that $g(0) = 0$ and $g(\pm\infty) = \pm\infty$. Substituting (3.7) into (3.1)–(3.3) and introducing the rescaled dependent variables

$$U_0 = U_e U, \quad V_0 = \theta^{-1}V + y_\xi U_0, \quad W_0 = \beta W, \quad \Omega_0 = \beta\theta^{-1}\Omega - y_\xi U_{0z}, \tag{3.8}$$

yields, after some manipulation,

$$\mathrm{D}U = 2\xi U U_\xi + \frac{1+3\mu}{2}U^2 - \mu, \tag{3.9}$$

$$\mathrm{D}\Omega = \xi U \Omega_\xi - \xi U_\zeta V_\xi + \frac{\xi}{g'}U_\eta W_\xi - 2(\kappa_\theta g + \kappa_\psi)U U_\zeta + \frac{1-\mu}{g'}U_{\eta\zeta}, \tag{3.10}$$

$$\Omega = \frac{1}{g'} W_\eta - V_\zeta, \tag{3.11}$$

$$\xi U_\xi + \frac{1+\mu}{2} U + \frac{1}{g'} V_\eta + \bar{\beta}^2 W_\zeta = 0, \tag{3.12}$$

where

$$\mathrm{D} \equiv \frac{\partial}{g' \partial \eta} \left(\frac{\partial}{g' \partial \eta} - V \right) + \bar{\beta}^2 \frac{\partial}{\partial \zeta} \left(\frac{\partial}{\partial \zeta} - W \right), \tag{3.13}$$

$\mu \equiv \theta^2 U_e'$ is the pressure-gradient parameter, $\bar{\beta} \equiv \theta\beta$ is the spanwise-wavenumber parameter, and $\kappa_\theta \equiv \theta^3 U_e^2 \theta''$ and $\kappa_\psi \equiv \theta^3 U_e^2 \psi''$ account for curvature effects associated with the displacement thickness and dividing stream surface, respectively.

Since (3.9)–(3.12) are parabolic in ξ, the base flow can be computed with a marching procedure starting at the streamwise position $\xi = \xi^0$. The solution is advanced in ξ using a combination of interpolation and finite-difference formulas,

$$f^{i+\varepsilon} = f(\xi^i + \varepsilon \Delta\xi, \eta, \zeta) = \varepsilon f^{i+1} + (1-\varepsilon) f^i + O(\Delta\xi^2), \tag{3.14}$$

$$f_\xi^{i+\varepsilon} = f_\xi(\xi^i + \varepsilon \Delta\xi, \eta, \zeta) = \Delta\xi^{-1} [(\varepsilon + \tfrac{1}{2}) f^{i+1} - 2\varepsilon f^i + (\varepsilon - \tfrac{1}{2}) f^{i-1}] + O(\Delta\xi^2), \tag{3.15}$$

which reproduce most of the familiar second-order accurate explicit and implicit schemes with appropriate choice of the parameter ε. In particular, a semi-implicit Crank–Nicolson scheme is obtained by setting $\varepsilon = \frac{1}{2}$ and a strongly implicit three-point-backward scheme results when $\varepsilon = 1$. All the computations in the present investigation were done with $\varepsilon = 1$.

The coupled set of nonlinear equations that determine $\{U^{i+1}, V^{i+1}, W^{i+1}, \Omega^{i+1}\}$ are linearized using a Newton–Raphson procedure,

$$U^{i+\varepsilon,n+1} = U^{i+\varepsilon,n} + \delta U, \tag{3.16}$$

$$V^{i+\varepsilon,n+1} = V^{i+\varepsilon,n} + \frac{1}{g'} \delta \Phi_\eta + \bar{\beta}^{2i+\varepsilon} \delta \Psi_\zeta, \tag{3.17}$$

$$W^{i+\varepsilon,n+1} = W^{i+\varepsilon,n} + \delta\Phi_\zeta - \frac{1}{g'}\delta\Psi_\eta, \tag{3.18}$$

$$\Omega^{i+\varepsilon,n+1} = \Omega^{i+\varepsilon,n} + \delta\Omega, \tag{3.19}$$

where the superscript n indicates the iteration number and, following Rubin *et al.* (1977), corrections to the velocity components in the transverse plane are expressed in terms of a velocity potential $\delta\Phi$ and a stream function $\delta\Psi$. Introducing (3.14)–(3.19) into (3.9)–(3.12) and linearizing about $\{\delta U, \delta\Phi, \delta\Psi, \delta\Omega\} = 0$ gives

$$\Delta\xi\left[\mathrm{D}^{i+\varepsilon} - \left(\frac{2\varepsilon+1}{\varepsilon\Delta\xi}\xi^{i+\varepsilon} + 1 + 3\mu^{i+\varepsilon}\right)U^{i+\varepsilon} - 2\xi^{i+\varepsilon}U_\xi^{i+\varepsilon}\right]\delta U = FU^{i+\varepsilon}, \tag{3.20}$$

$$\Delta\xi\left(\mathrm{D}^{i+\varepsilon} - \frac{2\varepsilon+1}{2\varepsilon\Delta\xi}\xi^{i+\varepsilon}U^{i+\varepsilon}\right)\delta\Omega = F\Omega^{i+\varepsilon}, \tag{3.21}$$

$$\Delta\xi\left(\mathrm{L}^{i+\varepsilon}\delta\Psi + \delta\Omega\right) = F\Psi^{i+\varepsilon}, \tag{3.22}$$

$$\Delta\xi\mathrm{L}^{i+\varepsilon}\delta\Phi = F\Phi^{i+\varepsilon}, \tag{3.23}$$

where

$$\mathrm{L} \equiv \frac{\partial}{g'\partial\eta}\left(\frac{\partial}{g'\partial\eta}\right) + \bar{\beta}^2\frac{\partial^2}{\partial\zeta^2}, \tag{3.24}$$

and the forcing functions FU, $F\Omega$, $F\Psi$ and $F\Phi$ are given in appendix A. The components of the transverse velocity, $V^{i+\varepsilon}$ and $W^{i+\varepsilon}$, in (3.20) and (3.21) have been lagged in the iteration (i.e. the $\delta\Phi$ and $\delta\Psi$ terms have been omitted) so that these equations decouple from (3.22) and (3.23). This allows an updated result for $U^{i+\varepsilon}$ to be computed from (3.20) prior to solving (3.21)–(3.23). Consequently, the δU terms in (3.21) and (3.23) have been omitted. The $\delta\Omega$ term in (3.22) has been retained because solving (3.21) and (3.22) as a coupled system greatly improves the convergence of the Newton–Raphson procedure for wall-bounded flows (Briley & McDonald 1984). In view of these considerations, the superscript n

has been dropped with the understanding that the latest iterates are used to evaluate terms at $\xi = \xi^{i+\epsilon}$.

Substituting (3.16)–(3.19) into (3.8) and the result together with (3.7) into the boundary conditions (3.5) and (3.6) shows that (3.20)–(3.23) must be solved subject to

$$\left.\begin{aligned} \{U,\ V,\ W,\ g'\Omega - W_\eta\} &= 0 \qquad \text{at} \quad \eta = 0 \\ \{U,\ V,\ W_\eta,\ \Omega\} &\to \{1,\ V^{(+)},\ 0,\ 0\} \quad \text{as} \quad \eta \to +\infty \end{aligned}\right\}, \tag{3.25a}$$

and

$$\left.\begin{aligned} \{\delta U,\ \delta\Phi_\eta,\ g'\delta\Phi_\zeta - \delta\Psi_\eta,\ \delta\Psi\} &= 0 \quad \text{at} \quad \eta = 0 \\ \{\delta U,\ \delta\Phi_{\eta\zeta},\ \delta\Psi,\ \delta\Omega\} &\to 0 \qquad \text{as} \quad \eta \to +\infty \end{aligned}\right\}, \tag{3.25b}$$

for wall-bounded flows,

$$\{U,\ V,\ W_\eta,\ \Omega\} \to \{(1 \pm U_e^{-2})^{1/2},\ V^{(\pm)},\ 0,\ 0\} \quad \text{as} \quad \eta \to \pm\infty, \tag{3.26a}$$

and

$$\{\delta U,\ \delta\Phi_{\eta\zeta},\ \delta\Psi,\ \delta\Omega\} \to 0 \quad \text{as} \quad \eta \to \pm\infty, \tag{3.26b}$$

for unbounded flows, and, in either case, $\{U, V, W, \Omega\}$ and $\{\delta U, \delta\Phi, \delta\Psi, \delta\Omega\}$ must be periodic in ζ with period 2π. The functions $V^{(\pm)}(\xi, \eta)$ appearing in these equations denote the rescaled normal-velocity components induced by the displacement thickness and are determined as part of the solution to (3.20)-(3.23) (see appendix A).

In view of the spanwise periodicity of the mean flow, the dependent variables in (3.20)-(3.23) are approximated by truncated Fourier series of the form

$$f(\xi^i, \eta, \zeta) \approx \tfrac{1}{2} \sum_{m=-M}^{+M} f_m(\xi^i, \eta) \mathrm{e}^{\mathrm{i}m\zeta}, \tag{3.27}$$

where

$$f_m \equiv \frac{1}{\pi} \int_{-\pi}^{+\pi} f \mathrm{e}^{-\mathrm{i}m\zeta} \mathrm{d}\zeta. \tag{3.28}$$

Derivatives in the normal direction are approximated with second-order-accurate central differences so,

$$f^i_{\eta m,j} = f_{\eta m}(\xi^i, \eta_j) = \tfrac{1}{2}\Delta\eta^{-1}(f^i_{m,j+1} - f^i_{m,j-1}) + O(\Delta\eta^2), \tag{3.29}$$

$$f^i_{\eta\eta m,j} = f_{\eta\eta m}(\xi^i, \eta_j) = \Delta\eta^{-2}(f^i_{m,j+1} - 2f^i_{m,j} + f^i_{m,j-1}) + O(\Delta\eta^2), \tag{3.30}$$

where $\eta_j = j\Delta\eta$. By introducing these approximations into (3.20)–(3.23), one obtains a system of algebraic equations that are expressed in matrix form as

$$\boldsymbol{BD}_j\boldsymbol{\delta U}_{j-1} + \boldsymbol{DU}_j\boldsymbol{\delta U}_j + \boldsymbol{AD}_j\boldsymbol{\delta U}_{j+1} = \boldsymbol{FU}^{i+\varepsilon}_j, \tag{3.31}$$

$$\boldsymbol{BD}_j\boldsymbol{\delta\Omega}_{j-1} + \boldsymbol{D\Omega}_j\boldsymbol{\delta\Omega}_j + \boldsymbol{AD}_j\boldsymbol{\delta\Omega}_{j+1} = \boldsymbol{F\Omega}^{i+\varepsilon}_j, \tag{3.32}$$

$$\boldsymbol{BL}_j\boldsymbol{\delta\Psi}_{j-1} + \boldsymbol{DL}_j\boldsymbol{\delta\Psi}_j + \boldsymbol{AL}_j\boldsymbol{\delta\Psi}_{j+1} + \Delta\xi\boldsymbol{\delta\Omega}_j = \boldsymbol{F\Psi}^{i+\varepsilon}_j, \tag{3.33}$$

$$\boldsymbol{BL}_j\boldsymbol{\delta\Phi}_{j-1} + \boldsymbol{DL}_j\boldsymbol{\delta\Phi}_j + \boldsymbol{AL}_j\boldsymbol{\delta\Phi}_{j+1} = \boldsymbol{F\Phi}^{i+\varepsilon}_j, \tag{3.34}$$

where $\boldsymbol{\delta U}_j \equiv \{\delta U_{m,j}\}$, $\boldsymbol{FU}_j \equiv \{FU_{m,j}\}, \ldots$ are column vectors of length $N \equiv 2M + 1$ and the non-zero elements of the order-N band matrices, $\boldsymbol{BD}_j$, $\boldsymbol{DU}_j$, $\boldsymbol{D\Omega}_j$, $\boldsymbol{AD}_j$, $\boldsymbol{BL}_j$, $\boldsymbol{DL}_j$ and $\boldsymbol{AL}_j$, are given in appendix A.

The LAPACK subroutine CGBSV is used to solve (3.31)–(3.34) subject to the boundary conditions obtained by introducing (3.27) and (3.29) into (3.25*b*) or (3.26*b*) (see appendix A). As mentioned above, (3.31) is solved first so that an updated result for $U^{i+\varepsilon}_{m,j}$ can be computed from (3.16) and used in the remaining equations. Equation (3.34) is solved next. For wall-bounded flows, this provides the result for $\delta\Phi$ needed to evaluate the $\delta\Psi$ boundary conditions and so enables the solution of the coupled system (3.32) and (3.33). For unbounded flows, the $\delta\Psi$ boundary conditions do not couple (3.32) to (3.33) so these equations can be solved *seriatum*. Updated results for $V^{i+\varepsilon}_{m,j}$, $W^{i+\varepsilon}_{m,j}$ and $\Omega^{i+\varepsilon}_{m,j}$ are then computed from (3.17)–(3.19)

and the solution procedure is repeated until the corrections $\{\delta U, \delta\Phi, \delta\Psi, \delta\Omega\}$ become less than a preset tolerance.

4. Unsteady perturbation

The rescaled equation that governs the shape function $\hat{p}$ is obtained by substituting the coordinate transformation (3.7) together with the rescaled variables (3.8) into (2.15) to get

$$(U-\bar{c})\left[\frac{1}{g'}\left(\frac{1}{g'}\hat{p}_\eta\right)_\eta+\bar{\beta}^2\hat{p}_{\zeta\zeta}-\bar{\alpha}^2\hat{p}\right]-\frac{2}{g'^2}U_\eta\hat{p}_\eta-2\bar{\beta}^2U_\zeta\hat{p}_\zeta=0, \tag{4.1}$$

where $\bar{\alpha}\equiv\theta\alpha$ and $\bar{c}\equiv c/U_e$ are the rescaled streamwise wavenumber and phase speed, respectively. In view of (2.16) and (2.17), (4.1) must be solved subject to

$$\hat{p}_\eta=0 \quad \text{at} \quad \eta=0, \quad \hat{p}\to 0 \quad \text{as} \quad \eta\to+\infty, \tag{4.2}$$

for wall-bounded flows, or

$$\hat{p}\to 0 \quad \text{as} \quad \eta\to\pm\infty, \tag{4.3}$$

for unbounded flows.

Since interest here is in disturbances that remain bounded as $z\to\pm\infty$ and since the mean flow is periodic in the spanwise direction, Floquet theory can be used to express the relevant solutions to (4.1) as a summation of solutions of the form

$$\hat{p}=\bar{p}(\eta,\zeta\,|\,\bar{\gamma})\mathrm{e}^{\mathrm{i}\bar{\gamma}\zeta}, \tag{4.4}$$

where $\bar{p}$ is periodic in ζ with period 2π and $\bar{\gamma}$ is a real characteristic exponent. Substituting (4.4) into (4.1), approximating U and $\bar{p}$ by truncated Fourier series of the form (3.27) and equating the coefficients of like powers of $\mathrm{e}^{\mathrm{i}\zeta}$ yields

$$\sum_{n=\max(-M,m-M)}^{\min(M,m+M)}\left\{(U_{m-n}-2\bar{c}\delta_{m,n})\left[\frac{1}{g'}\left(\frac{1}{g'}\bar{p}_{n\eta}\right)_\eta-\bar{\lambda}_n^2\bar{p}_n\right]\right.$$

$$- \frac{2}{g'^2} U_{m-n\eta} \bar{p}_{n\eta} + 2\bar{\beta}^2 (n+\bar{\gamma})(m-n) U_{m-n} \bar{p}_n \Big\} = 0, \qquad (4.5)$$

for $-M \leqslant m \leqslant +M$, where

$$\bar{\lambda}_m \equiv \left[\bar{\alpha}^2 + \bar{\beta}^2 (m+\bar{\gamma})^2 \right]^{1/2}, \quad \mathrm{Re}\, \bar{\lambda}_m > 0, \qquad (4.6)$$

and $\delta_{m,n}$ denotes the Kronecker delta. It follows from (3.25a), (3.26a), (4.2) and (4.3) that (4.5) must be solved subject to

$$\bar{p}_{m\eta} = 0 \quad \text{at} \quad \eta = 0, \quad \bar{p}_{m\eta} + \bar{\lambda}_m g' \bar{p}_m \to 0 \quad \text{as} \quad \eta \to +\infty, \qquad (4.7)$$

for wall-bounded flows, or

$$\bar{p}_{m\eta} \pm \bar{\lambda}_m g' \bar{p}_m \to 0 \quad \text{as} \quad \eta \to \pm\infty, \qquad (4.8)$$

for unbounded flows, where these expressions are obtained by using the exponential behavior of $\bar{p}_m$ in the free stream.

Introducing the central-difference approximations (3.29) and (3.30) into (4.5) leads to a system of algebraic equations that can be written in matrix form as

$$\boldsymbol{b}_j \bar{\boldsymbol{p}}_{j-1} + \boldsymbol{d}_j \bar{\boldsymbol{p}}_j + \boldsymbol{a}_j \bar{\boldsymbol{p}}_{j+1} = 0, \qquad (4.9)$$

where $\bar{\boldsymbol{p}}_j \equiv \{\bar{p}_{m,j}\}$ is a column vector of length $N \equiv 2M+1$ and $\boldsymbol{b}_j$, $\boldsymbol{d}_j$ and $\boldsymbol{a}_j$ are band matrices of order N. Away from the boundaries, the non-zero elements of $\boldsymbol{b}_j$, $\boldsymbol{d}_j$ and $\boldsymbol{a}_j$ are given by

$$b_{m,n,j} = \frac{1}{\Delta\eta^2} \left(1 + \frac{\Delta\eta}{2} \frac{g_j''}{g_j'} \right) \frac{1}{g_j'^2} (U_{m-n,j} - 2\bar{c}\delta_{m,n}) + \frac{1}{\Delta\eta} \frac{1}{g_j'^2} U_{m-n\eta_j}, \qquad (4.10)$$

$$d_{m,n,j} = - \left(\frac{2}{\Delta\eta^2} \frac{1}{g_j'^2} + \bar{\lambda}_n^2 \right) (U_{m-n,j} - 2\bar{c}\delta_{m,n}) + 2\bar{\beta}^2 (n+\bar{\gamma})(m-n) U_{m-n,j}, \qquad (4.11)$$

$$a_{m,n,j} = \frac{2}{\Delta\eta^2}\frac{1}{g_j'^2}(U_{m-n,j} - 2\bar{c}\delta_{m,n}) - b_{m,n,j}, \tag{4.12}$$

where $-M \leqslant m \leqslant +M$ and $\max(-M, m-M) \leqslant n \leqslant \min(M, m+M)$. Expressions for $b_{m,n,j}$, $d_{m,n,j}$ and $a_{m,n,j}$ at the boundaries are obtained from (4.7) or (4.8) by using (3.29) to approximate the η derivatives.

For a given base-flow profile U, Strouhal number S and characteristic exponent $\bar{\gamma}$, the rescaled wavenumber $\bar{\alpha}$ is determined by solving the eigenvalue problem (4.9). This is done with an iterative method similar to that used by Hughes (1972) to solve the Orr–Sommerfeld equation. The method is most easily applied when (4.9) is rewritten as

$$\boldsymbol{A}\,\boldsymbol{x} = 0, \tag{4.13}$$

where $x_{m+Nj} = \bar{p}_{m,j}$ and the non-zero elements of $\boldsymbol{A}$ are given by

$$A_{m+Nj,n+Nj-N} = b_{m,n,j}, \quad A_{m+Nj,n+Nj} = d_{m,n,j}, \quad A_{m+Nj,n+Nj+N} = a_{m,n,j}. \tag{4.14}$$

A normalization condition, $x_k = 1$ at $k = k_\star$, is imposed on $\boldsymbol{x}$ and the $k_\star$-th equation in (4.13) is relaxed by allowing

$$\sum_k A_{k_\star,k}x_k = \Delta \neq 0. \tag{4.15}$$

Equation (4.13) is then recast as an inhomogeneous problem by moving the terms involving $x_{k_\star}$ to the right-hand side and replacing the $k_\star$-th equation with the identity $x_{k_\star} = 1$. This yields

$$\boldsymbol{B}\boldsymbol{x} = \boldsymbol{f}, \tag{4.16}$$

where

$$B_{k,l} \equiv \delta_{k_\star,l}\delta_{k,k_\star} + (1-\delta_{k_\star,l})(1-\delta_{k,k_\star})A_{k,l}, \quad f_k \equiv \delta_{k,k_\star} - (1-\delta_{k,k_\star})A_{k,k_\star}. \tag{4.17}$$

Given an estimate for $\bar{\alpha}$, $\boldsymbol{x}$ is determined by solving the sparse linear system (4.16) with the LAPACK subroutine CGBSV. The eigenvalue $\bar{\alpha}$ is then found by locating the zeros of Δ using Newton's method.

5. Results and discussion

The generalized Rayleigh stability problem defined by (4.1)–(4.4) or equivalently (4.1)–(4.3) and the spanwise-boundary condition,

$$\hat{p}(\eta, \zeta + 2\pi \,|\, \bar{\gamma}) = \mathrm{e}^{\mathrm{i}2\pi\bar{\gamma}} \hat{p}(\eta, \zeta \,|\, \bar{\gamma}), \tag{5.1}$$

has a number symmetries with respect to the characteristic exponent $\bar{\gamma}$ that are used to simplify the numerical computations. Let $\{\hat{p}(\eta, \zeta \,|\, \bar{\gamma}), \bar{\alpha}(\bar{\gamma})\}$ denote an eigenfunction/eigenvalue pair determined for a particular value of $\bar{\gamma}$, it then follows from (5.1) that there exists an infinite sequence of eigenpairs $\{\hat{p}(\eta, \zeta \,|\, \bar{\gamma} + k), \bar{\alpha}(\bar{\gamma} + k)\}$ such that

$$\hat{p}(\eta, \zeta \,|\, \bar{\gamma} + k) = \hat{p}(\eta, \zeta \,|\, \bar{\gamma}) \quad \text{and} \quad \bar{\alpha}(\bar{\gamma} + k) = \bar{\alpha}(\bar{\gamma}), \tag{5.2}$$

where $k = 0, \pm 1, \pm 2, \ldots$. If the base-flow profile U is an even function of ζ as it will now be assumed, there also exists an eigenpair $\{\hat{p}(\eta, \zeta \,|\, -\bar{\gamma}), \bar{\alpha}(-\bar{\gamma})\}$ such that

$$\hat{p}(\eta, -\zeta \,|\, -\bar{\gamma}) = \hat{p}(\eta, \zeta \,|\, \bar{\gamma}) \quad \text{and} \quad \bar{\alpha}(-\bar{\gamma}) = \bar{\alpha}(\bar{\gamma}). \tag{5.3}$$

Combining this result with (5.2) leads to

$$\hat{p}(\eta, -\zeta \,|\, 1 - \bar{\gamma}) = \hat{p}(\eta, \zeta \,|\, \bar{\gamma}) \quad \text{and} \quad \bar{\alpha}(1 - \bar{\gamma}) = \bar{\alpha}(\bar{\gamma}). \tag{5.4}$$

Therefore, only solutions for $\bar{\gamma}$ in the range 0 to $\frac{1}{2}$ need be computed since solutions outside this range can be easily obtained from (5.2)–(5.4).

The ζ symmetries of the solutions to the generalized Rayleigh stability problem are also of interest. Let the eigenfunction $\hat{p}(\eta, \zeta \,|\, \bar{\gamma})$ be expressed as

$$\hat{p}(\eta, \zeta \,|\, \bar{\gamma}) = \hat{p}_o(\eta, \zeta \,|\, \bar{\gamma}) + \hat{p}_e(\eta, \zeta \,|\, \bar{\gamma}), \tag{5.5}$$

where $\hat{p}_o$ and $\hat{p}_e$ are odd and even functions of ζ, respectively. Then, since U is an even function of ζ, $\hat{p}_o$ and $\hat{p}_e$ satisfy (4.1)–(4.3) independently but are coupled through the spanwise-boundary condition (5.1). This coupling becomes clear when (5.5) is used to rewrite (5.1) as

$$\hat{p}_o(\eta, \zeta + 2\pi \,|\, \bar{\gamma}) = \cos(2\pi\bar{\gamma})\hat{p}_o(\eta, \zeta \,|\, \bar{\gamma}) + \mathrm{i}\sin(2\pi\bar{\gamma})\hat{p}_e(\eta, \zeta \,|\, \bar{\gamma}), \tag{5.6a}$$

and

$$\hat{p}_e(\eta, \zeta + 2\pi \,|\, \bar{\gamma}) = \mathrm{i}\sin(2\pi\bar{\gamma})\hat{p}_o(\eta, \zeta \,|\, \bar{\gamma}) + \cos(2\pi\bar{\gamma})\hat{p}_e(\eta, \zeta \,|\, \bar{\gamma}). \tag{5.6b}$$

It follows that the coupling terms in (5.6) drop out whenever $\bar{\gamma} = \frac{1}{2}k$. $\hat{p}_o$ and $\hat{p}_e$ are then independent solutions to the generalized Rayleigh stability problem which (together with their corresponding eigenvalues) are termed odd- and even-mode solutions.

The numerical computations discussed below are for wall-bounded flows so the function $\psi(\xi)$ introduced in (3.7) is identically zero. The stretching function $g(\eta)$ used in the computations is given as

$$g = \left(\frac{\Delta\eta \sinh A\eta}{\sinh A\Delta\eta} + \mathrm{i}B\right) \tanh\left(C\,\frac{\Delta\eta \sinh A\eta}{\sinh A\Delta\eta}\right), \tag{5.7}$$

where A, B, and C are real constants. Typical values for these constants are $A \approx 5.5 \times 10^{-6}\Delta\eta^{-1}$, $B = -0.4$ and $C = 10$ when the computation is done off the real axis and $A \approx 5.5 \times 10^{-6}\Delta\eta^{-1}$, $B = 0$ and $C = \infty$ when it is done on the real axis.

Figure 1 is a comparison of the scaled growth rate $-\theta\alpha_i/\sigma^4$ predicated by the long-wavelength solution developed in GW (and extended in appendix B) to that determined

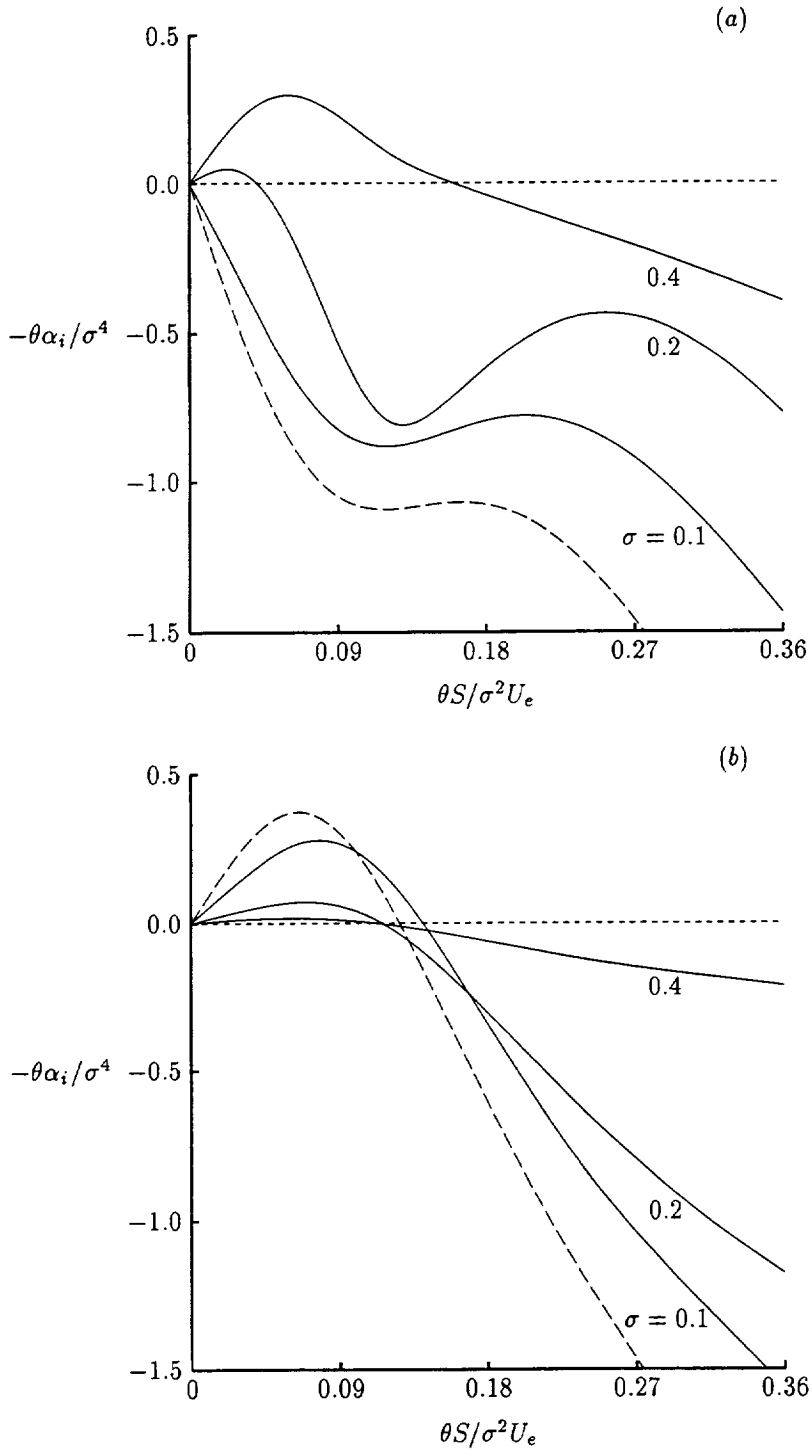

Figure 1: Scaled growth rate *vs.* scaled Strouhal number for U given by (5.8), $\theta\beta/\sigma = \frac{1}{2}$, $\bar{\gamma} = \frac{1}{2}$ and various values of σ. Solid lines, exact numerical solution; dashed lines, long-wavelength asymptotic solution. (*a*) odd mode; (*b*) even mode.

from a corresponding numerical solution to the generalized Rayleigh stability problem for the analytic base-flow profile

$$U = U_B(g) - \sigma^3 g e^{-g^3/5\sigma^3} \cos\zeta, \tag{5.8}$$

where $0 < \sigma \ll 1$ is a scale factor and U_B is the Blasius profile determined by

$$U_B'' - V_B U_B' = 0 \quad \text{and} \quad \tfrac{1}{2} U_B + V_B' = 0, \tag{5.9}$$

with $U_B(0) = V_B(0) = 0$ and $U_B(\infty) = 1$. The computations were performed with the grid parameters $\Delta\eta = 0.001$, $J = 1500$ and $N = 27$. The curves are plotted for both odd- and even-mode solutions at $\bar{\gamma} = \frac{1}{2}$. At the largest value of σ, the exact and asymptotic results appear quite different. The exact solutions show a relatively fast growing odd mode and a weakly unstable even mode whereas the asymptotic results predict a completely damped odd mode and a rapidly growing even mode. However, this disparity diminishes and the exact solutions approach their respective asymptotes as $\sigma \to 0$.

Figure 2 is a plot of the scaled growth rate $-\theta\alpha_i/\sigma^4$ as a function of the characteristic exponent $\bar{\gamma}$ for the analytic base-flow profile (5.8). The curves are plotted for a scaled Strouhal number $\theta S/\sigma^2 U_e = 0.06$ which is near the peak in the asymptotic growth rate of the even mode at $\bar{\gamma} = \frac{1}{2}$. Also shown are the growth rates predicted by the long-wavelength solutions (B 46) and (B 47) which have been evaluated with $\sigma = 0.1$. The results plotted in parts *a* and *b* of the figure correspond to solutions that become, respectively, odd and even functions of ζ when $\bar{\gamma} = \frac{1}{2}$. As noted above, the odd and even mode designations apply only when $\bar{\gamma} = \frac{1}{2}k$. Indeed, these designations change as $\bar{\gamma}$ is decreased from $\frac{1}{2}$ to 0, i.e. the solution that corresponds to an odd mode at $\bar{\gamma} = \frac{1}{2}$ becomes an even function of ζ when $\bar{\gamma} = 0$ and *vice versa* for the solution that corresponds to an even mode at $\bar{\gamma} = \frac{1}{2}$.

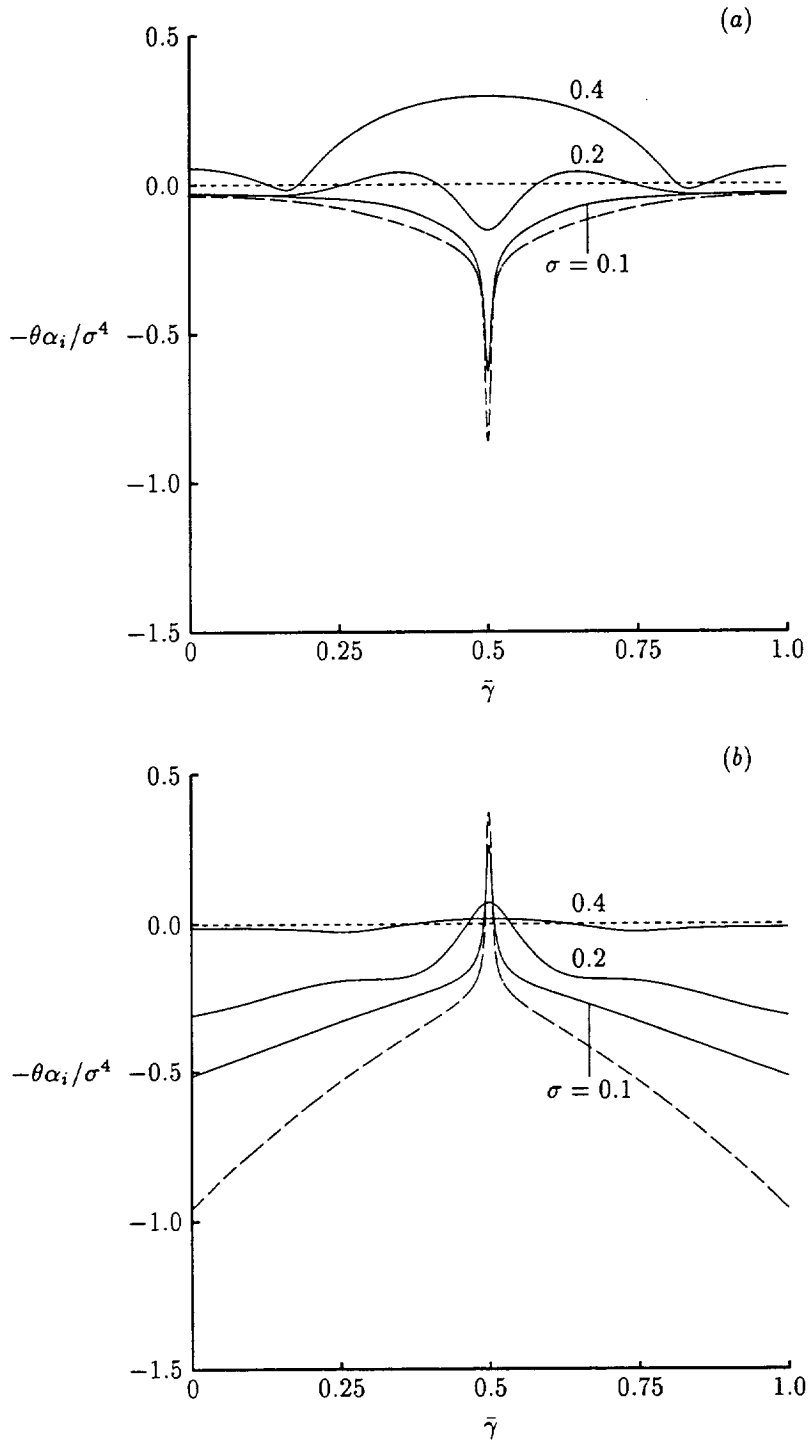

Figure 2: Scaled growth rate *vs.* characteristic exponent for U given by (5.8), $\theta\beta/\sigma = \frac{1}{2}$, $\theta S/\sigma^2 U_e = 0.06$ and various values of σ. Solid lines, exact numerical solution; dashed lines, long-wavelength asymptotic solution. (*a*) solution that is odd mode at $\bar{\gamma} = \frac{1}{2}$; (*b*) solution that is even mode at $\bar{\gamma} = \frac{1}{2}$.

As in figure 1, the exact and asymptotic solutions in figure 2 appear quite different at the largest value of σ but come into agreement as σ decreases. It is interesting to note that the solution for $\sigma = 0.2$ shown in figure 2*a* is damped at $\bar{\gamma} = 0$ and $\frac{1}{2}$ but is unstable when $\bar{\gamma}$ is near 0.35. This points out the need for investigating more than just the fundamental and subharmonic solutions to the generalized Rayleigh stability problem. Figure 2 also shows that the effect of the streamwise-vortex structure on the instability waves becomes concentrated near $\bar{\gamma} = \frac{1}{2}$ as σ becomes small which is consistent with the conclusions in GW. This means that, once σ becomes sufficiently small, the base flow is inviscidly unstable only to subharmonic disturbances.

Figures 1 and 2 are plotted for a scaled spanwise wavenumber $\theta\beta/\sigma = \frac{1}{2}$. In order to demonstrate the effect of this parameter on the linear-stability results, the neutral (or zero-growth) values of the scaled Strouhal number $\theta S/\sigma^2 U_e$ predicted by the long-wavelength solution are plotted against $\theta\beta/\sigma$ in figure 3 for both odd- and even-mode solutions at $\bar{\gamma} = \frac{1}{2}$. The figure shows that there are multiple ranges of $\theta\beta/\sigma$ over which the profile (5.8) is inviscidly unstable. However, each range is finite so above a certain value of $\theta\beta/\sigma$ (5.8) becomes inviscidly stable even though it remains inflexional over a portion of the spanwise domain. This is consistent with the experimental observations of Hamilton & Abernathy (1994) who investigated the conditions under which transition to turbulence can be caused by introducing streamwise vortices into an otherwise two-dimensional, non-transitional shear flow. Figure 3 suggests that growing solutions exist when $\theta\beta/\sigma = 0$. This result must be disregarded because the analysis of GW shows that the long-wavelength asymptotic solution breaks down as $\beta \to 0$ with $\sigma > 0$ held constant. In order to show that the above conclusions apply to other base-flow profiles, a plot of the neutral Strouhal number *versus* the spanwise

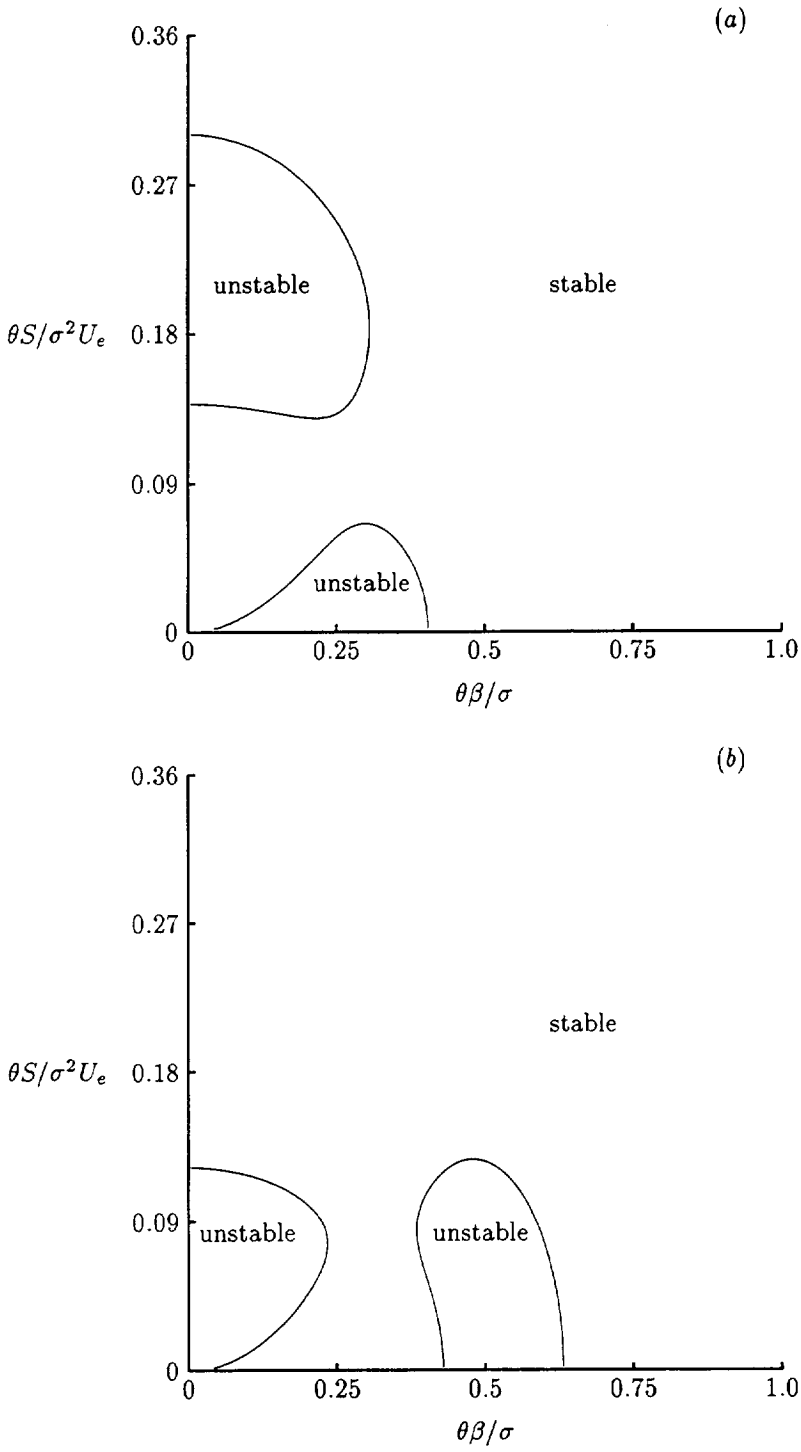

Figure 3: Scaled neutral Strouhal number *vs.* scaled spanwise wavenumber for the long-wavelength asymptotic solution with U given by (5.8) and $\bar{\gamma} = \frac{1}{2}$. (*a*) odd mode; (*b*) even mode.

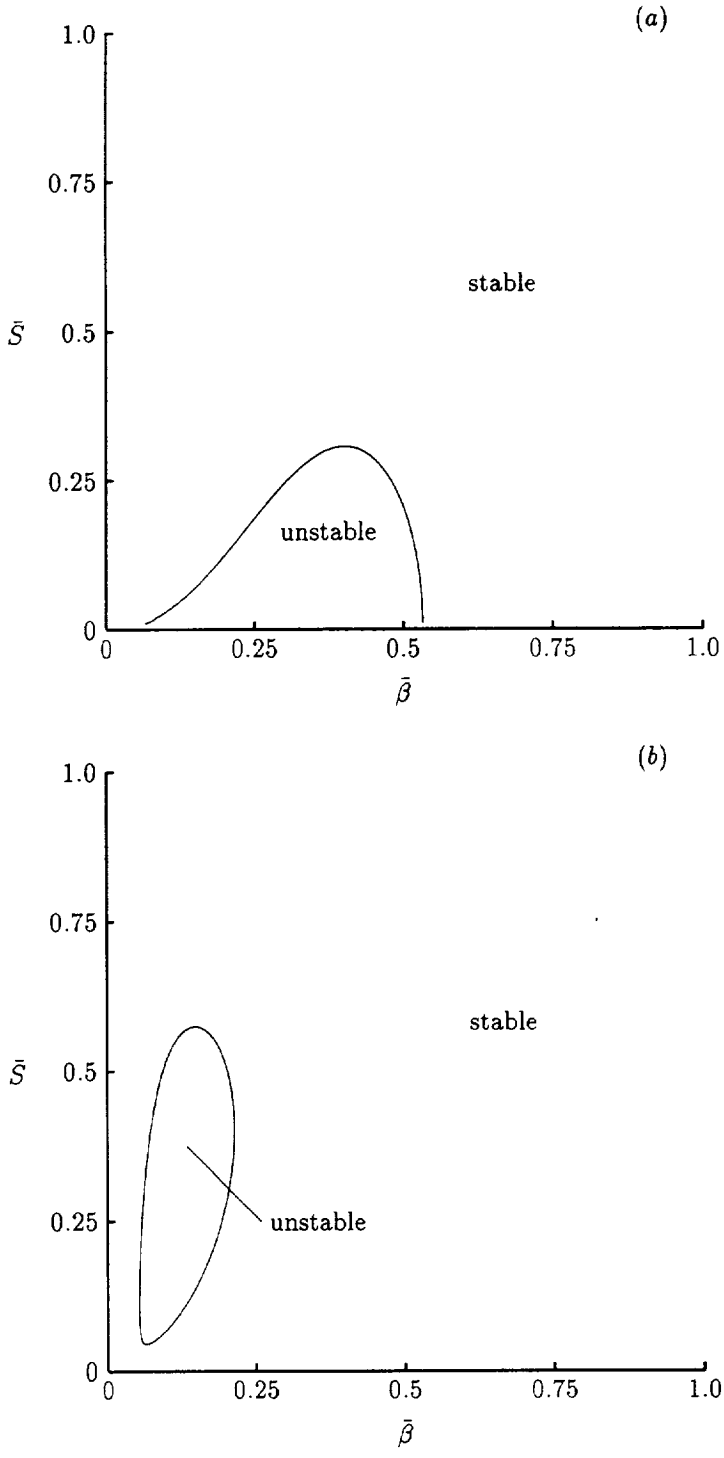

Figure 4: Scaled neutral Strouhal number *vs.* scaled spanwise wavenumber in the notation of GW for the long-wavelength asymptotic solution with $\bar{\gamma} = \frac{1}{2}$ and U given by (3.32), (3.43) and (3.51) of GW where $\sigma = 0.05$, $\mathcal{B}_0 = -16\,\pi$ and $\lambda = 0$. (*a*) odd mode; (*b*) even mode.

wavenumber is shown in figure 4 for the base-flow profile derived in GW.

The time needed to compute curves corresponding to figure 3 for the exact solutions to the generalized Rayleigh equation would be prohibitive. However, the results in figures 1 and 2 suggest that, at small values of σ, qualitatively similar curves would be obtained. It is unlikely that this similarity would persist as σ increases but it is interesting to note that, in their numerical investigation of the secondary instability of Görtler vortices, Li & Malik (1995) found that the relative growth rates of the odd and even modes are strongly influenced by the Görtler-vortex wavelength (i.e. the spanwise wavelength of the base flow).

The influence of non-parallel-flow effects is demonstrated by computing the local stability characteristics of a base-flow profile U that satisfies the boundary-region equations (3.9)–(3.12). The computation is done for a wall-bounded flow with $U_e = 1$ and

$$U = U_B, \quad V = V_B + \bar{\beta}^2 U_B H_\zeta, \quad W = -U_B H_g, \quad \Omega = -(U_B H_g)_g - \bar{\beta}^2 U_B H_{\zeta\zeta}, \tag{5.10}$$

at $\xi = \xi^0 = 1$, where U_B and V_B satisfy (5.9), $\bar{\beta} = \sqrt{\xi}$, and the function $H(\eta, \zeta)$ is given as

$$H = \lambda_B^{-4} U_B U_B' \sin\zeta, \tag{5.11}$$

with $\lambda_B \equiv U_B'(0)$. The form of the 'initial' condition (5.10) has been chosen so that U, V, and W satisfy the equation obtained by eliminating the U_ξ terms between (3.9) and (3.12). Equations (3.9)–(3.12) are solved subject to (3.25) and (5.10) using the method described in §3 with $\Delta\xi = 0.001$, $\Delta\eta = 0.005$, $J = 900$ and $N = 17$.

Figure 5 shows lines of constant streamwise velocity U in the g–ζ plane at various streamwise stations. The contours at $\xi = 1$ are not shown but, in view of (5.10), they would be straight lines parallel to the ζ axis. The contours in parts a–e of figure 5 reveal a rapid departure from the initial two-dimensional state as the distortion in U produced

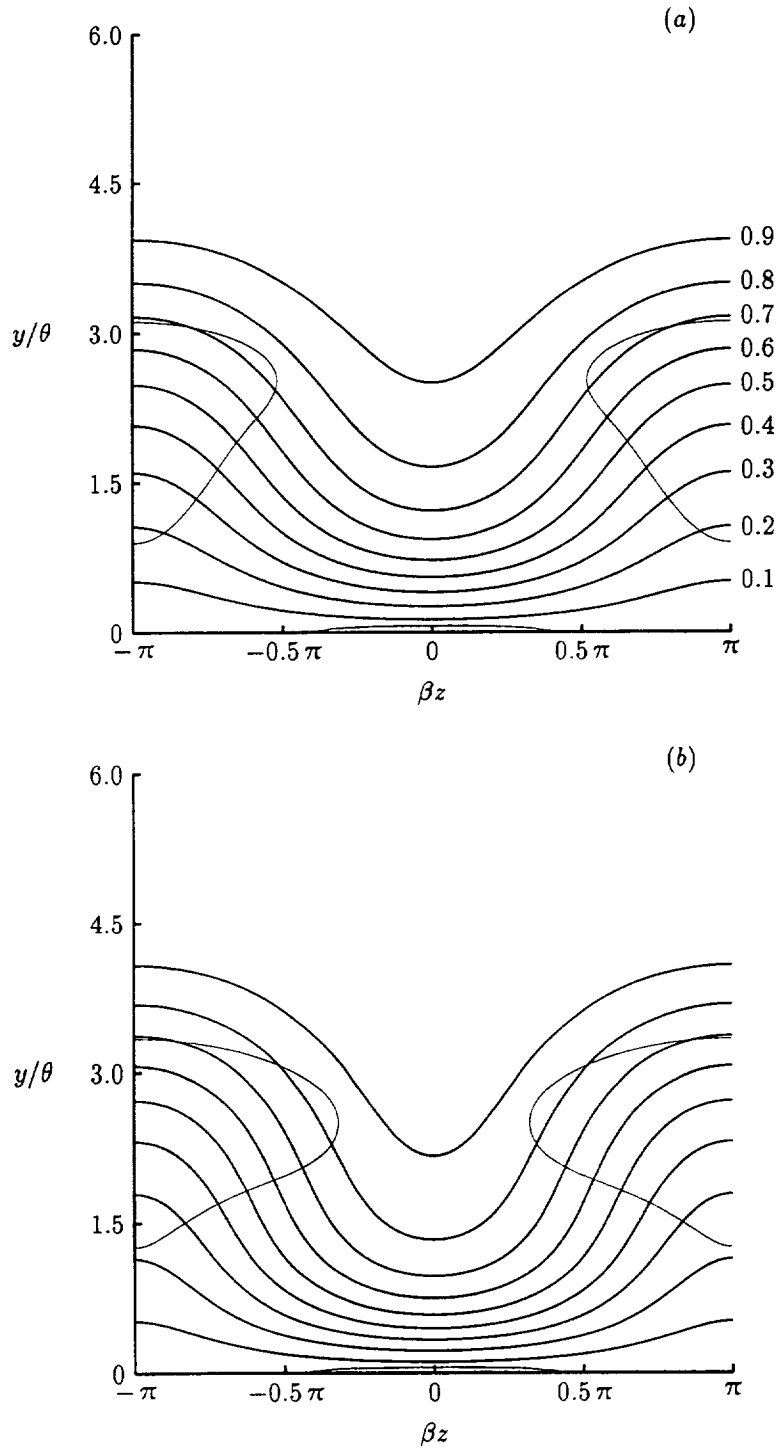

Figure 5: Streamwise velocity contours in the g–ζ plane. Thick lines, U contours; thin lines, inflexion points. (*a*) $\xi = 1.1$; (*b*) $\xi = 1.15$; (*c*) $\xi = 1.2$; (*d*) $\xi = 1.3$; (*e*) $\xi = 1.5$; (*f*) $\xi = 1.8$.

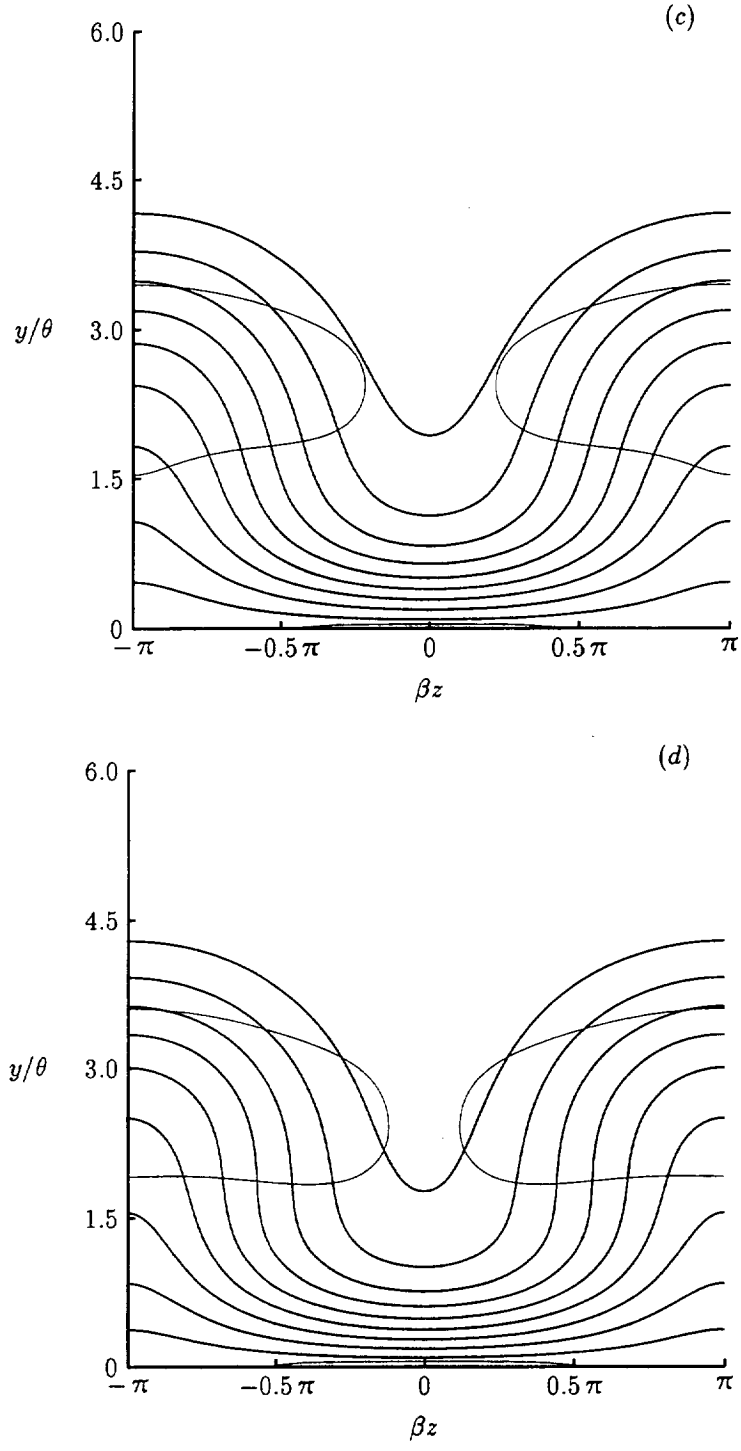

Figure 5: Streamwise velocity contours in the g–ζ plane. Thick lines, U contours; thin lines, inflexion points. (*a*) $\xi = 1.1$; (*b*) $\xi = 1.15$; (*c*) $\xi = 1.2$; (*d*) $\xi = 1.3$; (*e*) $\xi = 1.5$; (*f*) $\xi = 1.8$.

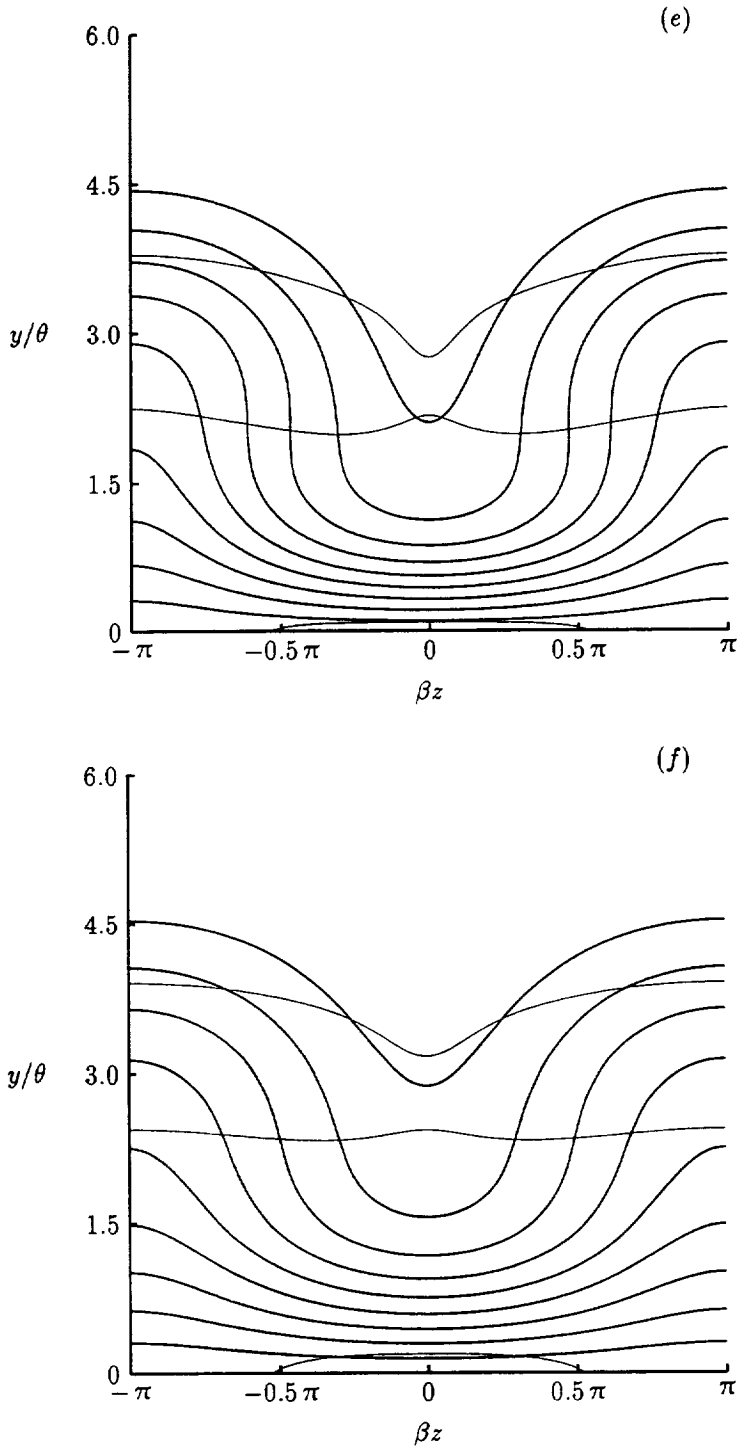

Figure 5: Streamwise velocity contours in the g–ζ plane. Thick lines, U contours; thin lines, inflexion points. (*a*) $\xi = 1.1$; (*b*) $\xi = 1.15$; (*c*) $\xi = 1.2$; (*d*) $\xi = 1.3$; (*e*) $\xi = 1.5$; (*f*) $\xi = 1.8$.

by the imposed cross flow grows with increasing ξ. This type of disturbance growth is similar to the algebraic growth proposed by Ellingsen & Palm (1975), Hultgren & Gustavsson (1981) and Landahl (1990) as an alternative or 'bypass' transition mechanism. However, only the base-flow distortion undergoes this type of growth in the present study and the follow-on secondary instability (discussed below) exhibits the more conventional exponential growth. The wavy appearance of the contours in figure 5 is similar that observed in the early stages of Görtler-vortex development (Swearingen & Blackwelder 1987). The 'mushroom-like' structures characteristic of the later stages of that development do not appear in figure 5 because the vortex structure shown there is not sustained by wall-curvature effects. The growth of the U distortion in the present study is eventually reversed by viscous-diffusion effects and the base flow tends towards its two-dimensional undisturbed state as ξ becomes large (cf. figure 5*f*).

Figure 5 also shows the location of the inflection points in the U–g plane, i.e. the points where $U_{gg} = 0$. Wundrow & Goldstein (1994) showed that the connection between the inflexions in U and the stability of the base flow is much more complicated for a transversely sheared base flow of the kind being considered here than for a plane flow for which Rayleigh's inflexion-point theorem applies. Nevertheless the inflexions in U do indicate a redistribution in momentum produced by the streamwise-vortex structure that does play a role in determining the local stability of the flow.

Figure 6 is a plot of the local instability-wave growth rate $-\theta\alpha_i$ against the local Strouhal number $\theta S/U_e$ for the base-flow profile U shown in figure 5. Growth rate curves are shown for odd-fundamental ($\bar{\gamma} = 0$, odd-mode) and even-subharmonic ($\bar{\gamma} = \frac{1}{2}$, even-mode) solutions. Curves for even-fundamental and odd-subharmonic solutions are not shown since only

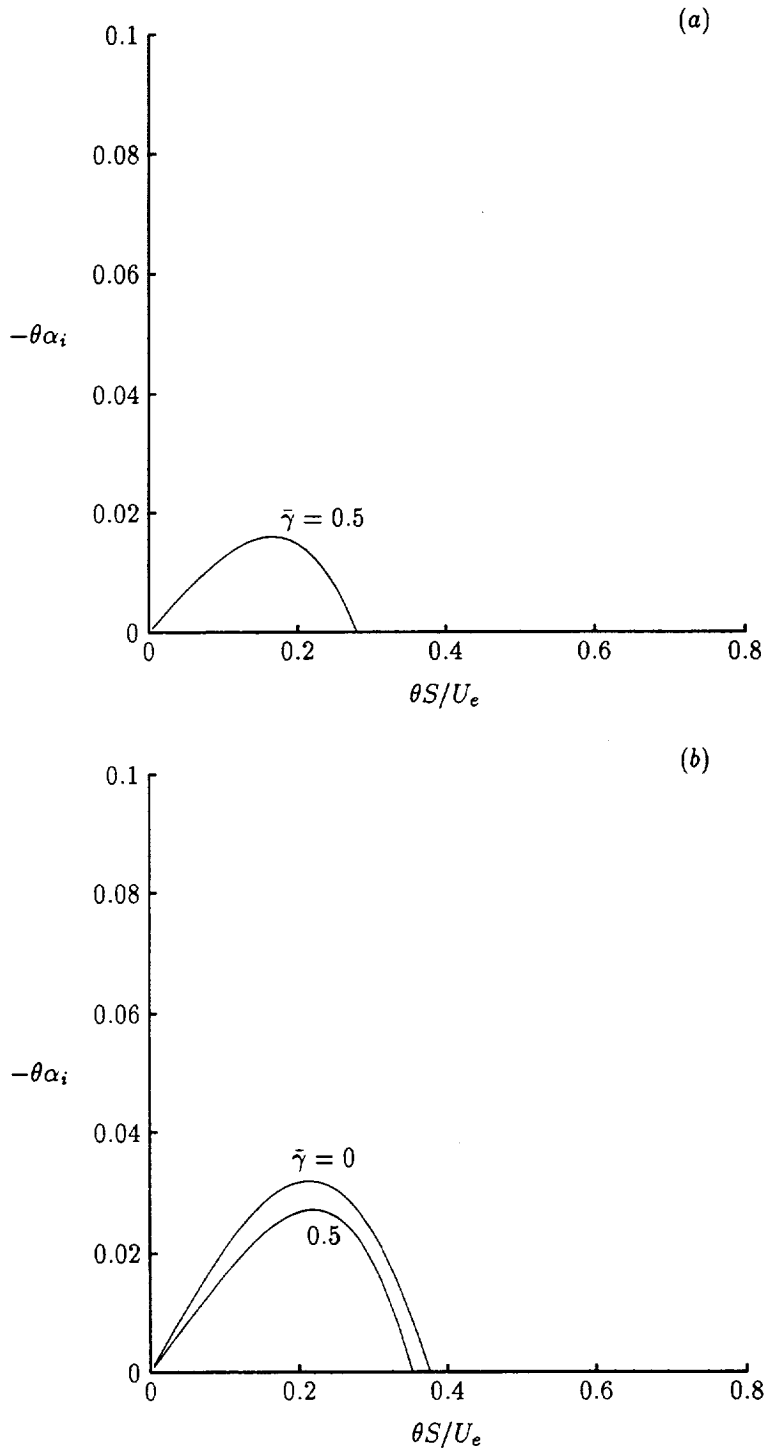

Figure 6: Local growth rate *vs.* local Strouhal number for computed U. (a) $\xi = 1.1$; (b) $\xi = 1.15$; (c) $\xi = 1.2$; (d) $\xi = 1.3$; (e) $\xi = 1.5$; (f) $\xi = 1.8$.

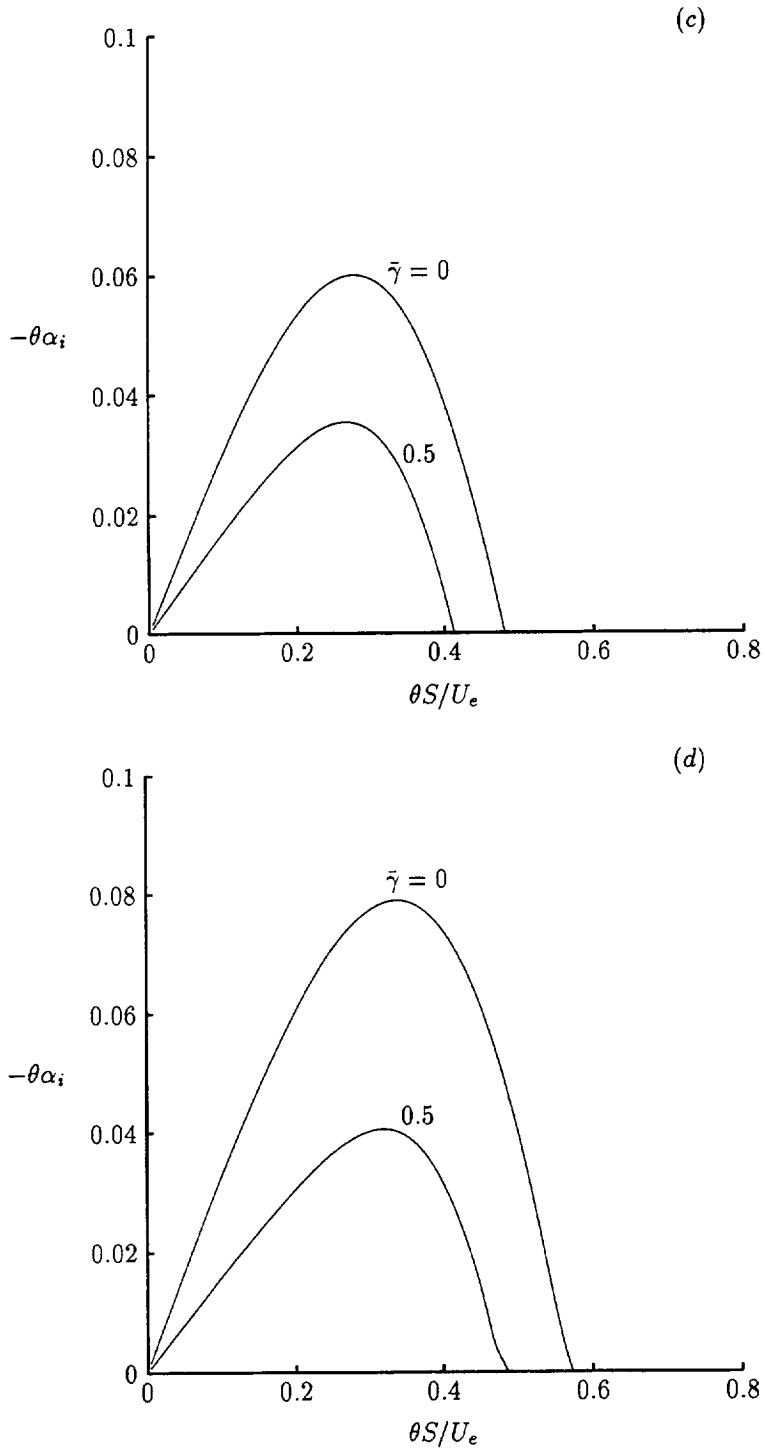

Figure 6: Local growth rate *vs.* local Strouhal number for computed U. (*a*) $\xi = 1.1$; (*b*) $\xi = 1.15$; (*c*) $\xi = 1.2$; (*d*) $\xi = 1.3$; (*e*) $\xi = 1.5$; (*f*) $\xi = 1.8$.

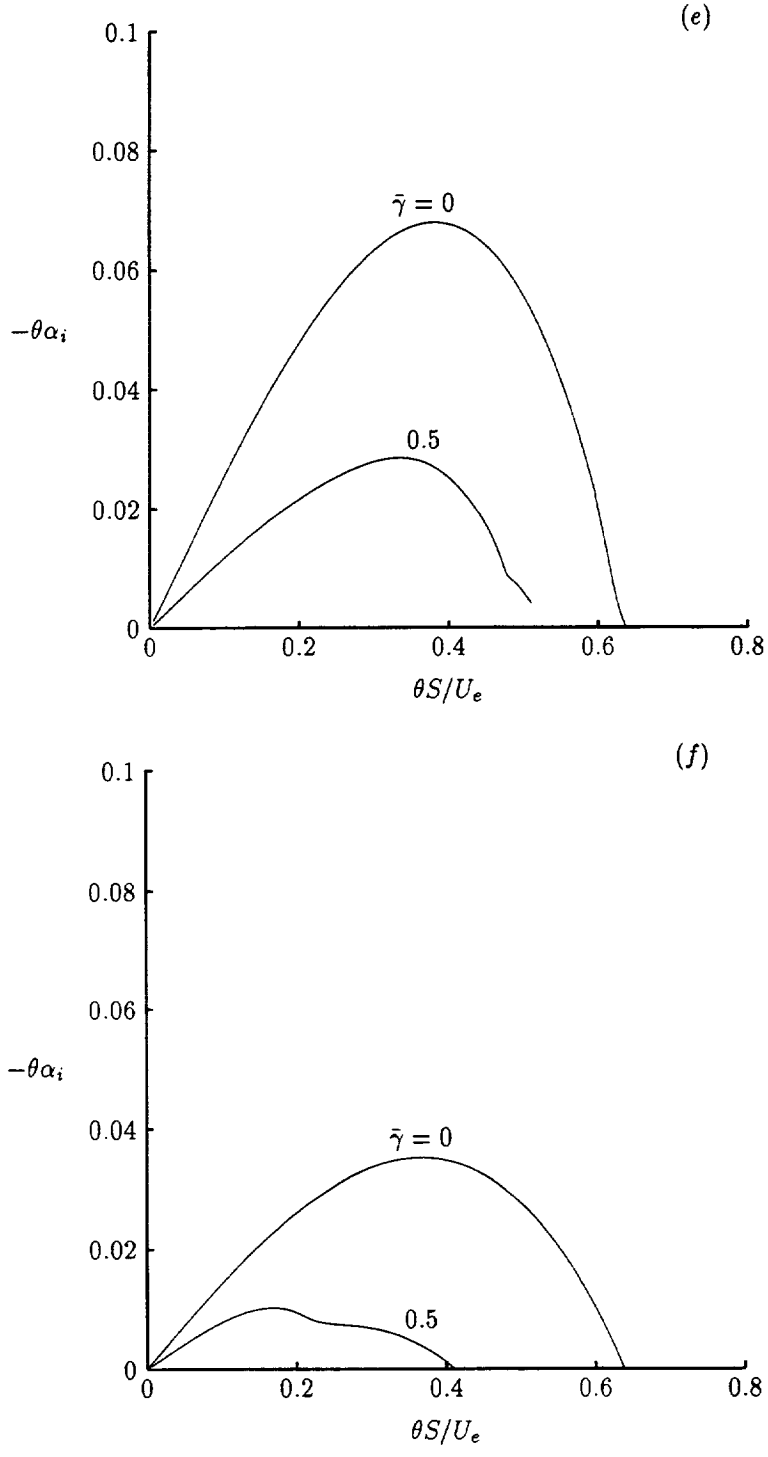

Figure 6: Local growth rate *vs.* local Strouhal number for computed U. (*a*) $\xi = 1.1$; (*b*) $\xi = 1.15$; (*c*) $\xi = 1.2$; (*d*) $\xi = 1.3$; (*e*) $\xi = 1.5$; (*f*) $\xi = 1.8$.

damped forms of these solutions were found. It should be noted that the shooting method used here does not determine all the eigenvalues of the generalized Rayleigh stability problem and a global method must be applied to show that there are no unstable even-fundamental or odd-subharmonic solutions. In figure 6*a*, only the even-subharmonic solution is shown because the odd-fundamental solution is damped at this streamwise station. This suggests that at short distances (on the x_2 scale) downstream of the point where the cross flow is introduced the linear instability of the flow is dominated by a subharmonic rather than a fundamental solution. This is also the case in the long-wavelength analysis considered in GW. Further downstream, as the U distortion becomes larger, the odd-fundamental solution becomes unstable and soon exhibits a peak growth rate larger than that of the even-subharmonic solution. The growth rates of both solutions continue to increase until $\xi \approx 1.3$ after which point they decrease with increasing ξ. It is interesting to note that the streamwise position of peak growth precedes the position were the U distortion is a maximum. This behavior is also evident in the long-wavelength asymptotic solution developed by GW.

Figures 5 and 6 show that the imposed cross flow (5.10) produces a streamwise region in which the boundary layer is inviscidly unstable. In order to show that this region of instability can significantly affect the boundary-layer development, an estimate of its streamwise extent is made using the flow parameters reported in Swearingen & Blackwelder (1987). In their experimental investigation of the evolution of Görtler vortices, Swearingen & Blackwelder introduced a small-amplitude acoustic disturbance 60 cm downstream of the leading edge of a concave plate and observed vortex breakdown leading to laminar–turbulent transition at downstream distances between 100 and 110 cm. Taking $L_* = 60$ cm and using $\xi^0 \equiv L_*/R\delta_* = 1$ together with (2.6) and (3.7), the dimensional distance from the leading edge

in the present investigation is

$$x_* + L_* = R\delta_* \xi = 60\,\xi \text{ cm}.$$

Therefore, since ξ ranges between 1.1 and 1.8 in figures 5 and 6, the distance over which the imposed cross flow (5.10) destabilizes the boundary layer is the same as the distance over which the secondary instability of Görtler vortices leads to laminar–turbulent transition in the Swearingen & Blackwelder (1987) experiment.

The ability of a given streamwise-vortex structure to significantly affect the development of an otherwise two-dimensional shear flow will, of course, depend on the vortex strength. The strength of the streamwise-vortex structure can be characterized by its circulation,

$$\Gamma \equiv \frac{1}{2\pi}\int_0^{\pi/\beta}\int_0^{\infty} \Omega_0 \mathrm{d}y\mathrm{d}z = -\frac{1}{2\pi}\int_0^{\infty}\left[V + \tfrac{1}{2}(1-\mu)gU\right]_{\zeta=0}^{\pi}\mathrm{d}g, \qquad (5.12)$$

where use has been made of (3.3), (3.5), (3.7) and (3.8). The non-dimensional circulation (or vortex Reynolds number) Γ of the imposed cross flow (5.10) is approximately 9 – well within the range of vortex strength considered in the experimental investigation of Hamilton & Abernathy (1994). Vortex structures of lesser strength were also found to destabilize the boundary layer but the streamwise distance over which this occured tended to be smaller. Concentrating the imposed cross flow near the wall was found to reduce the streamwise distance needed to achieve an inflexional U profile but again the resulting vortex structures tended to damp out sooner. Changing the spanwise wavelength of the vortex structure was found to alter the linear stability characteristics however further investigation is need to verify if behavior such as that shown in figures 3 and 4 occurs in the order-one wavelength case.

The results presented here show that the introduction of even a very weak streamwise-vortex structure into an otherwise two-dimensional boundary layer can lead to the amplification of certain three-dimensional disturbances through a kind of parametric-resonance or secondary-instability mechanism. The amplification rates of these secondary instabilities are strongly dependent on their spanwise wavelength as well as the strength and spanwise wavelength of the streamwise-vortex structure. Nevertheless, at sufficiently high Reynolds numbers, the secondary instabilities can grow at a rate much faster than that of the Tollmien–Schlichting waves which would otherwise dominate the initial stages of laminar–turbulent transition. Viscous effects eventually damp out the base-flow distortion and consequently any instability wave amplified by it. However, the damping process occurs over the relatively long x_2 scale so an initially linear instability wave can easily become nonlinear before this process is complete.

Nonlinear effects will become important first within a thin critical layer located at the transverse position where the phase speed $\bar{c}$ of the instability wave equals the base-flow velocity U (once the instability-wave amplitude and growth rate become sufficiently large and small, respectively). The unsteady flow outside the critical layer remains essentially linear but the instability-wave amplitude is then completely determined by the nonlinear motion inside the critical layer. An analysis of this stage of evolution is given in GW for the long wavelength limit and in Wundrow & Goldstein (1994) for the order-one wavelength problem considered here. It is worth noting (as pointed out by Hultgren 1992) that the near-neutral approximation used in the order-one-wavelength critical-layer analysis will remain accurate even at frequencies close to the peak growth because the slope of the growth rate curve between that point and the upper branch is nearly constant (cf. figure 6).

Appendix A. Coefficients and boundary conditions for (3.31)–(3.34)

In this appendix, expressions are given for the forcing terms, matrix elements and boundary conditions associated with the algebraic equations (3.31)–(3.34). The forcing terms are defined as

$$FU \equiv -\Delta\xi \left(\mathrm{D}U - 2\xi U U_\xi - \frac{1+3\mu}{2} U^2 + \mu \right), \tag{A 1}$$

$$F\Omega \equiv -\Delta\xi \left[\mathrm{D}\Omega - \xi U \Omega_\xi + \xi U_\zeta V_\xi - \frac{\xi}{g'} U_\eta W_\xi + 2(\kappa_\theta g + \kappa_\psi) U U_\zeta - \frac{1-\mu}{g'} U_{\eta\zeta} \right], \tag{A 2}$$

$$F\Psi \equiv -\Delta\xi \left(\Omega - \frac{1}{g'} W_\eta + V_\zeta \right), \tag{A 3}$$

$$F\Phi \equiv -\Delta\xi \left(\xi U_\xi + \frac{1+\mu}{2} U + \frac{1}{g'} V_\eta + \bar{\beta}^2 W_\zeta \right), \tag{A 4}$$

where it should be noted that these terms vanish when $\{U, V, W, \Omega\}$ satisfy (3.9)–(3.12). The non-zero matrix elements are given by

$$BL_{m,n,j} = BD_{m,n,j} - \frac{\Delta\xi}{4\Delta\eta} \frac{1}{g'_j} V^{i+\varepsilon}_{m-n,j-1} = \delta_{m,n} \frac{\Delta\xi}{\Delta\eta^2} \left(1 + \frac{\Delta\eta}{2} \frac{g''_j}{g'_j} \right) \frac{1}{g'^2_j}, \tag{A 5}$$

$$DL_{m,n,j} = DD_{m,n,j} + \frac{\Delta\xi}{2} \bar{\beta}^{2i+\varepsilon} \mathrm{i} m W^{i+\varepsilon}_{m-n,j} = -\delta_{m,n} \Delta\xi \left(\frac{2}{\Delta\eta^2 g'^2_j} + \bar{\beta}^{2i+\varepsilon} m^2 \right), \tag{A 6}$$

$$AL_{m,n,j} = AD_{m,n,j} + \frac{\Delta\xi}{4\Delta\eta} \frac{1}{g'_j} V^{i+\varepsilon}_{m-n,j+1} = \delta_{m,n} \frac{\Delta\xi}{\Delta\eta^2} \left(1 - \frac{\Delta\eta}{2} \frac{g''_j}{g'_j} \right) \frac{1}{g'^2_j}, \tag{A 7}$$

$$DU_{m,n,j} = DD_{m,n,j} - \left(\frac{2\varepsilon+1}{2\varepsilon} \xi^{i+\varepsilon} + \frac{1+3\mu^{i+\varepsilon}}{2} \Delta\xi \right) U^{i+\varepsilon}_{m-n,j} - \Delta\xi\, \xi^{i+\varepsilon} U^{i+\varepsilon}_{\xi_{m-n,j}}, \tag{A 8}$$

$$D\Omega_{m,n,j} = DD_{m,n,j} - \frac{2\varepsilon+1}{4\varepsilon} \xi^{i+\varepsilon} U^{i+\varepsilon}_{m-n,j}, \tag{A 9}$$

where $-M \leqslant m \leqslant +M$, $\max(-M, m-M) \leqslant n \leqslant \min(M, m+M)$, $\delta_{m,n}$ denotes the Kronecker delta and dependent variables with superscript $i+\varepsilon$ are evaluated using (3.14) and (3.15).

Setting $\Delta\eta \equiv \eta_{\max}/J$ and introducing (3.27) and (3.29) into (3.25) and (3.26) shows that, in algebraic form, the normal-boundary conditions read

$$U_{m,0} = V_{m,0} = W_{m,0} = 0, \quad W_{m,-1} = W_{m,1} - 2\Delta\eta g_0' \Omega_{m,0},$$

$$U_{m,J} = 2\delta_{m,0}, \quad mV_{m,J} = 0, \quad W_{m,J+1} = W_{m,J-1}, \quad \Omega_{m,J} = 0, \tag{A 10a}$$

and

$$\delta U_{m,0} = \delta\Psi_{m,0} = 0, \quad \delta\Phi_{m,-1} = \delta\Phi_{m,1}, \quad \delta\Psi_{m,-1} = \delta\Psi_{m,1} - 2\mathrm{i}m\Delta\eta g_0' \delta\Phi_{m,0},$$

$$\delta U_{m,J} = \delta\Psi_{m,J} = \delta\Omega_{m,J} = 0, \quad m\delta\Phi_{m,J+1} = m\delta\Phi_{m,J-1}, \tag{A 10b}$$

for wall-bounded flows, and

$$U_{m,\pm J} = 2\delta_{m,0}(1 \pm U_e^{-2})^{1/2}, \quad mV_{m,\pm J} = 0, \quad W_{m,\pm J\pm 1} = W_{m,\pm J\mp 1}, \quad \Omega_{m,\pm J} = 0, \tag{A 11a}$$

and

$$\delta U_{m,\pm J} = \delta\Psi_{m,\pm J} = \delta\Omega_{m,\pm J} = 0, \quad m\delta\Phi_{m,\pm J\pm 1} = m\delta\Phi_{m,\pm J\mp 1}, \tag{A 11b}$$

for unbounded flows. The normalization condition

$$\delta\Phi_{0,0} = 0, \tag{A 12}$$

and, in the case of unbounded flows, the kinematic condition

$$\delta\Phi_{0,1} = \delta\Phi_{0,-1}, \tag{A 13}$$

must also be imposed on the solution in order to uniquely determine $\delta\Phi_{0,j}$. These conditions allow the $m = 0$ component of (3.34) to be solved as an initial-value problem. With $\delta\Phi_{0,j}$ so determined, the normal-velocity components $V^{(\pm)}$ induced by the displacement thickness can be found from (3.17).

By substituting (3.27), (3.29) and (3.30) into (3.18) and the η-derivative of (3.17) and combining the results with (A 10) and (A 11), the following supplemental expressions are obtained,

$$V_{m,-1} = V_{m,1}, \tag{A 14}$$

$$\delta V_{m,J+1} = \delta V_{m,J-1} + f_J(\delta\Phi_{m,J-1} - \delta\Phi_{m,J}) - f_J h_J^{-1}(\delta\Phi_{m,J-1} - \delta\Phi_{m,J+1}) - \mathrm{i}m\bar{\beta}^{2i+\epsilon} h_J \delta\Psi_{m,J-1}, \tag{A 15}$$

$$\delta W_{m,J} = \mathrm{i}m\delta\Phi_{m,J} + \tfrac{1}{8} f_J h_J \delta\Psi_{m,J-1}, \tag{A 16}$$

for wall-bounded flows, and

$$\delta V_{m,\pm J\pm 1} = \delta V_{m,\pm J\mp 1} \pm f_{\pm J}(\delta\Phi_{m,\pm J\mp 1} - \delta\Phi_{m,\pm J}) \mp f_{\pm J} h_{\pm J}^{-1}(\delta\Phi_{m,\pm J\mp 1} - \delta\Phi_{m,\pm J\pm 1}) - \mathrm{i}m\bar{\beta}^{2i+\epsilon} h_{\pm J}\delta\Psi_{m,\pm J\mp 1}, \tag{A 17}$$

$$\delta W_{m,\pm J} = \mathrm{i}m\delta\Phi_{m,\pm J} \pm \tfrac{1}{8} f_{\pm J} h_{\pm J}\delta\Psi_{m,\pm J\mp 1}, \tag{A 18}$$

for unbounded flows, where

$$\delta V \equiv \frac{1}{g'}\delta\Phi_\eta + \bar{\beta}^{2i+\epsilon}\delta\Psi_\zeta, \quad \delta W \equiv \delta\Phi_\zeta - \frac{1}{g'}\delta\Psi_\eta,$$

$$f_{\pm J} \equiv \frac{4}{\Delta\eta g'_{\pm J}}, \quad \text{and} \quad h_{\pm J} \equiv \frac{4g'_{\pm J}}{2g'_{\pm J} \mp \Delta\eta g''_{\pm J}}.$$

These expressions are used when computing updated results for $V_{m,j}^{i+\epsilon}$ and $W_{m,j}^{i+\epsilon}$ at the η boundaries.

Appendix B. Long-wavelength solution to (4.1) and (4.2)

In this appendix, an asymptotic solution to the generalized Rayleigh stability problem (4.1) and (4.2) that applies in the limit as $\bar{\beta} \to 0$ is constructed. The analysis closely parallels

that given in GW but is carried out here for shape functions $\hat{p}$ having the general Floquet form (4.4). The relevant wavenumber and phase speed scalings for the long-wavelength limit are

$$\bar{\beta} = \sigma\tilde{\beta}, \quad \bar{\alpha} = \sigma\tilde{\alpha} = \sigma\tilde{\alpha}_r + \mathrm{i}\sigma^4\tilde{\alpha}_i, \quad \bar{c} = \sigma\tilde{c} = \sigma\tilde{c}_r + \mathrm{i}\sigma^4\tilde{c}_i, \tag{B 1}$$

where $0 < \sigma \ll 1$ is a scale factor, $\tilde{\beta}$ is an order-one real constant and the real quantities $\tilde{\alpha}_r$, $\tilde{\alpha}_i$, $\tilde{c}_r$ and $\tilde{c}_i$ have expansions of the form

$$\tilde{\alpha}_r = \tilde{\alpha}_{r0} + \sigma\tilde{\alpha}_{r1} + \cdots, \tag{B 2}$$

as $\sigma \to 0$.

As in GW, the present analysis is restricted to wall-bounded flows that behave like small perturbations about the Blasius solution. In the streamwise region of interest, the streamwise velocity of the base flow is then expressed as

$$U = U_B + \sigma^4 U_D, \tag{B 3}$$

where U_B corresponds to the Blasius solution determined by (5.9) and U_D is a spanwise-periodic distortion. Introducing (B 1) into (4.1) and (4.2) leads to

$$\left[\frac{\hat{p}_g}{(U-\sigma\tilde{c})^2}\right]_g + \sigma^2\tilde{\beta}^2\left[\frac{\hat{p}_\zeta}{(U-\sigma\tilde{c})^2}\right]_\zeta - \sigma^2\tilde{\alpha}^2\frac{\hat{p}}{(U-\sigma\tilde{c})^2} = 0, \tag{B 4}$$

and

$$\hat{p}_g = 0 \quad \text{at} \quad g = 0, \quad \hat{p} \to 0 \quad \text{as} \quad g \to +\infty, \tag{B 5}$$

where, for convenience, g is treated as an independent variable.

Since much of the analysis in GW carries over directly, only the final results are presented here. In the inviscid wall layer described by $\tilde{g} \equiv \sigma^{-1}g = O(1)$, the base flow is given as

$$U = \sigma\lambda_B\tilde{g} + \sigma^4\left(\tilde{U} - \tfrac{1}{48}\lambda_B^2\tilde{g}^4\right) + \cdots, \tag{B 6}$$

where $\lambda_B \equiv U_B'(0)$ and $\tilde{U}(\tilde{g},\zeta;\sigma) \equiv U_D(\sigma\tilde{g},\zeta;\sigma) = O(1)$. The shape function $\hat{p}$ is given by

$$\hat{p} = \sigma A + O(\sigma^5) \tag{B 7a}$$

and

$$\frac{\hat{p}_{\tilde{g}}}{(U-\sigma\tilde{c}_r)^2} = \frac{\sigma^3}{\lambda_B^2}\mathcal{D}\left[\frac{\tilde{g}}{\tilde{g}_c(\tilde{g}-\tilde{g}_c)}\right] + \frac{\sigma^6}{\lambda_B^3}\mathcal{D}\left[\Phi + \tilde{\mu}(\phi^{\pm}-\phi^{-}) - \frac{\mathrm{i}\tilde{c}_i\tilde{g}^2}{\tilde{g}_c^2(\tilde{g}-\tilde{g}_c)^2}\right] + \cdots, \tag{B 7b}$$

where A is an arbitrary function of ζ that has an expansion in σ containing terms up to but not including order σ^4, $\mathcal{D} \equiv \tilde{\beta}^2(A_\zeta\partial/\partial\zeta + A_{\zeta\zeta}) - \tilde{\alpha}^2 A$, the normal position of the critical level, $g_c = \sigma\tilde{g}_c$, is determined by the condition

$$U(g_c,\zeta;\sigma) = \sigma\tilde{c}_r, \tag{B 8}$$

the $\pm$ superscript indicates different values for $\tilde{g} \gtrless \tilde{g}_c$, a subscript c denotes evaluation at $\tilde{g} = \tilde{g}_c$, Φ is a real function of $\tilde{g}$ and ζ defined as

$$\Phi \equiv \fint_0^{\tilde{g}} \frac{\tilde{U} - \tilde{U}_c - \frac{1}{48}\lambda_B^2(\tilde{g}^4 - \tilde{g}_c^4)}{\frac{1}{2}(\tilde{g}-\tilde{g}_c)^3}\mathrm{d}\tilde{g}, \tag{B 9}$$

$\fint$ denotes the Cauchy principal value, and

$$\tilde{\mu} \equiv \tilde{U}_{\tilde{g}\tilde{g}c} - \tfrac{1}{4}\lambda_B^2\tilde{g}_c^2 \tag{B 10}$$

is the scaled normal derivative of the base-flow vorticity at the critical level. The constant $\phi^+ - \phi^-$ is set equal to $\mathrm{i}\pi$ which corresponds to a logarithmic phase shift of π across the linear critical layer.

In order to obtain solutions for $\hat{p}$ of the form (4.4) that are valid for all $\bar{\gamma}$, it is necessary to retain some intermediate terms (which were not needed in the GW analysis) in the main-boundary-layer and outer-layer solutions. In the main boundary layer described by $g = O(1)$,

the solution for $\hat{p}$ is given, to the required order of accuracy, by

$$\hat{p} = \sigma A + \sigma^2 \int_0^g (U_B - \sigma\tilde{c}_r)^2 \left[(1-\sigma^2 J\mathcal{L})\mathcal{D}B - \sigma(I-\sigma^2 K\mathcal{L})\mathcal{L}A\right] \mathrm{d}g + \cdots, \qquad \text{(B 11)}$$

where B is a function of ζ that has an expansion in σ containing terms up to but not including order σ^4, $\mathcal{L} \equiv \tilde{\beta}^2\partial^2/\partial\zeta^2 - \tilde{\alpha}^2$ and I, J and K are the real functions of g determined by

$$(U_B - \sigma\tilde{c}_r)^2 I' = 1, \quad \text{and} \quad [(U_B - \sigma\tilde{c}_r)^2\{J,K\}]' = (U_B - \sigma\tilde{c}_r)^2\{1,I\}, \qquad \text{(B 12)}$$

with $\{I, J, J', K, K'\} = 0$ at $g = 0$. Matching (B 11) with the wall-layer solution (B 7) shows that

$$B = \lambda_B^{-1}\tilde{c}_r^{-1} + \sigma^3\omega, \qquad \text{(B 13)}$$

where ω is a complex function of ζ defined as

$$\omega \equiv \lambda_B^{-3} \lim_{\tilde{g}\to\infty} \left[\Phi + \tfrac{1}{4}\lambda_B^2(\tfrac{1}{12}\tilde{g}^2 + \tfrac{1}{2}\tilde{g}_c\tilde{g} + \tilde{g}_c^2 \ln\sigma\tilde{g}) + \mathrm{i}\,\pi\tilde{\mu} - \tfrac{1}{48}\tilde{c}_r^2\right] + \lambda_B^{-1}\tilde{c}_r^{-2}(\tilde{U}_c - \mathrm{i}\tilde{c}_i), \quad \text{(B 14)}$$

and use has been made of the small-σ expansion

$$\tilde{g}_c = \lambda_B^{-1}\tilde{c}_r - \sigma^3(\lambda_B^{-1}\tilde{U}_c - \tfrac{1}{48}\lambda_B^{-3}\tilde{c}_r^4) + \cdots, \qquad \text{(B 15)}$$

which is easily obtained from (B 6) and (B 8).

In the outer layer described by $\bar{g} \equiv \sigma g = O(1)$, the solution for $\hat{p}$ expands like

$$\hat{p} = \sigma\tilde{p} + O(\sigma^5), \qquad \text{(B 16)}$$

where the function $\tilde{p}$ of $\bar{g}$ and ζ is determined by the Helmholtz equation,

$$\tilde{p}_{\bar{g}\bar{g}} + \tilde{\beta}^2\tilde{p}_{\zeta\zeta} - \tilde{\alpha}^2\tilde{p} = 0, \qquad \text{(B 17)}$$

which must be solved subject to

$$\tilde{p} = (1 + \sigma\nu_2\mathcal{L} - \sigma^3\nu_4\mathcal{L}^2)A, \quad \tilde{p}_{\bar{g}} = (\nu_1\mathcal{L} - \sigma^2\nu_3\mathcal{L}^2)A + \sigma^3\mathcal{D}\omega, \quad \text{at} \quad \bar{g} = 0, \qquad \text{(B 18}a\text{)}$$

in order for (B 16) to match with the main-boundary-layer solution (B 11) and

$$\tilde{p} \to 0 \quad \text{as} \quad \bar{g} \to +\infty \tag{B 18b}$$

in order to satisfy the free-stream boundary condition. The ν_n appearing in (B 18a) are real constants defined as

$$\lambda_B \tilde{c}_r I'_\infty \{\nu_1, \nu_2, \nu_3, \nu_4\} \equiv \{\, 1 - \sigma\lambda_B \tilde{c}_r I_\infty,\ J'_\infty - \sigma\lambda_B \tilde{c}_r K'_\infty,\ J_\infty - \sigma\lambda_B \tilde{c}_r K_\infty,\ L_\infty\}, \tag{B 19}$$

where

$$I_\infty \equiv \lim_{g\to\infty}(I - I'_\infty g), \quad I'_\infty \equiv (1 - \sigma\tilde{c}_r)^{-2}, \tag{B 20}$$

$$J_\infty \equiv \lim_{g\to\infty}(J - \tfrac{1}{2}g^2 - J'_\infty g), \quad J'_\infty \equiv \lim_{g\to\infty}(J' - g), \tag{B 21}$$

$$K_\infty \equiv \lim_{g\to\infty}(K - \tfrac{1}{6}I'_\infty g^3 - \tfrac{1}{2}I_\infty g^2 - K'_\infty g), \quad K'_\infty \equiv \lim_{g\to\infty}(K' - \tfrac{1}{2}I'_\infty g^2 - I_\infty g), \tag{B 22}$$

and

$$L_\infty \equiv \int_0^\infty [(U_B - \sigma\tilde{c}_r)^2 I'_\infty J - \tfrac{1}{2}g^2 - J'_\infty g - J_\infty]\mathrm{d}g. \tag{B 23}$$

The relevant solutions to (B 17) and (B 18) have the form

$$\{\tilde{p}, A\} = \tfrac{1}{2}\sum_{m=-\infty}^{+\infty} \{\tilde{p}_m \mathrm{e}^{-\tilde{\lambda}_m \tilde{g}}, A_m\}\mathrm{e}^{\mathrm{i}(m+\bar{\gamma})\zeta}, \tag{B 24}$$

where $\bar{\gamma}$ is the real characteristic exponent. It follows from (B 14), (B 17), (B 18) and (B 24) that

$$\tilde{\lambda}_m = \left[\tilde{\alpha}^2 + \tilde{\beta}^2(m + \bar{\gamma})^2\right]^{1/2}, \quad \mathrm{Re}\,\tilde{\lambda}_m > 0, \tag{B 25}$$

$$\tilde{p}_m = (1 - \sigma\nu_2\tilde{\lambda}_m^2 - \sigma^3\nu_4\tilde{\lambda}_m^4)A_m, \tag{B 26}$$

and

$$b_m A_{m-1} + d_m A_m + a_m A_{m+1} = 0, \tag{B 27}$$

where

$$b_m \equiv \sigma^3 \tfrac{1}{8}\omega_1(\tilde{\lambda}_{m-2}^2 - 4\tilde{\lambda}_{m-1}^2 - \tilde{\lambda}_m^2), \tag{B 28}$$

$$d_m \equiv \tilde{\lambda}_m - (\nu_1 + \tfrac{1}{2}\sigma^3\omega_0)\tilde{\lambda}_m^2 - \sigma\nu_2\tilde{\lambda}_m^3 - \sigma^2\nu_3\tilde{\lambda}_m^4 - \sigma^3\nu_4\tilde{\lambda}_m^5, \tag{B 29}$$

$$a_m \equiv -\sigma^3 \tfrac{1}{8}\omega_1(\tilde{\lambda}_m^2 + 4\tilde{\lambda}_{m+1}^2 - \tilde{\lambda}_{m+2}^2), \tag{B 30}$$

$$\omega_m \equiv \frac{1}{\pi}\int_{-\pi}^{+\pi} \omega \mathrm{e}^{-\mathrm{i}m\zeta}\mathrm{d}\zeta, \tag{B 31}$$

and, in order to fix ideas, it has been assumed that U_D is proportional to $\cos\zeta$. Equations (B 25)–(B 27) together with the definition of the scaled Strouhal number,

$$\tilde{S} \equiv \tilde{\alpha}\tilde{c} = \frac{\theta}{\sigma^2 U_e}S, \quad \mathrm{Im}\,\tilde{S} = 0, \tag{B 32}$$

form the eigenvalue problem that determines $\tilde{\alpha}$ as a function of $\tilde{S}$, $\tilde{\beta}$ and $\bar{\gamma}$.

The small-σ behavior of $\tilde{\alpha}$ is determined by using the method of cyclic reduction to express (B 27) as

$$-b_{m-1}b_m d_{m+1}A_{m-2} + (d_{m-1}d_m d_{m+1} - a_{m-1}b_m d_{m+1} - d_{m-1}a_m b_{m+1})A_m$$
$$- d_{m-1}a_m a_{m+1}A_{m+2} = 0, \tag{B 33}$$

and then imposing the normalization condition $A_0 = 1$ so that attention is restricted to instability waves having the bulk of their energy in the $m = 0$ mode. Equations (B 28)–(B 30) together with (B 33) show that $A_{\pm 2} = O(\sigma^3)$ and therefore that

$$d_{-1}d_0d_1 - a_{-1}b_0d_1 - d_{-1}a_0b_1 = O(\sigma^9), \tag{B 34}$$

which, to the required level of approximation, is the characteristic equation for (B 27).

The solutions for $\tilde{\alpha}$ that are of most interest here are those corresponding to instability waves having spanwise wavelengths nearly twice that of the base flow since it is in this

parameter range that the waves exhibit their most rapid growth. Substituting

$$\bar{\gamma} = \tfrac{1}{2} + \sigma^3 h, \tag{B 35}$$

into (B 25) and the result into (B 28)–(B 30) yields

$$b_m = -\sigma^3 \tfrac{1}{2}\omega_1 \left[\tilde{k}_m^2 - \tilde{\beta}^2(m+\tfrac{1}{2})\right] + O(\sigma^6), \tag{B 36}$$

$$\begin{aligned} d_m = {} & \tilde{k}_m - (\nu_1 + \tfrac{1}{2}\sigma^3\omega_0)\tilde{k}_m^2 - \sigma\nu_2\tilde{k}_m^3 - \sigma^2\nu_3\tilde{k}_m^4 - \sigma^3\nu_4\tilde{k}_m^5 \\ & - \sigma^3(2m+1)(\nu_1 - \tfrac{1}{2}\tilde{k}_m^{-1})\tilde{\beta}^2 h + O(\sigma^4), \end{aligned} \tag{B 37}$$

$$a_m = -\sigma^3 \tfrac{1}{2}\omega_1 \left[\tilde{k}_m^2 + \tilde{\beta}^2(m+\tfrac{1}{2})\right] + O(\sigma^6), \tag{B 38}$$

where

$$\tilde{k}_m = \left[\tilde{\alpha}^2 + \tilde{\beta}^2(m+\tfrac{1}{2})^2\right]^{1/2}, \quad \operatorname{Re}\tilde{k}_m > 0. \tag{B 39}$$

Then, since $\tilde{k}_{-1} = \tilde{k}_0$ and the $m = 0$ component of (B 27) implies $d_0 = O(\sigma^3)$, substitution of (B 36)–(B 38) into (B 34) leads to

$$\begin{aligned} & \left[\tilde{k}_0 - (\nu_1 + \tfrac{1}{2}\sigma^3\omega_0)\tilde{k}_0^2 - \sigma\nu_2\tilde{k}_0^3 - \sigma^2\nu_3\tilde{k}_0^4 - \sigma^3\nu_4\tilde{k}_0^5\right]^2 = \\ & \qquad \left[\sigma^3\tfrac{1}{2}\omega_1(\tilde{k}_0^2 - \tfrac{1}{2}\tilde{\beta}^2)\right]^2 + \left[\sigma^3(\nu_1 - \tfrac{1}{2}\tilde{k}_0^{-1})\tilde{\beta}^2 h\right]^2 + O(\sigma^7). \end{aligned} \tag{B 40}$$

Substituting (B 1) and (B 2) into (B 39) and the result into (B 40) and equating like powers of σ shows that

$$\left(\tilde{\alpha}_{r0}^2 + \tfrac{1}{4}\tilde{\beta}^2\right)^{1/2} = \lambda_B \tilde{c}_{r0} \tag{B 41a}$$

and

$$\left(\cos\tilde{\theta} + \frac{1}{\cos\tilde{\theta}}\right)\tilde{\alpha}_{i0} = \frac{\pi\tilde{c}_{r0}^4}{4\lambda_B} \pm \operatorname{Im}\left[(\tfrac{1}{2}\lambda_B^2\tilde{c}_{r0}^2\omega_1\cos 2\tilde{\theta})^2 + (\tilde{\beta}h\sin\tilde{\theta})^2\right]^{1/2}, \tag{B 41b}$$

where $\tilde{\theta} \equiv \arctan(\tilde{\beta}/2\tilde{\alpha}_{r0})$ is the obliqueness angle of the instability wave and it follows from (B 9), (B 14) and (B 31) that

$$\omega_1 = \frac{1}{\pi \lambda_B^3} \int_{-\pi}^{+\pi} \left[\int_0^{\infty} \frac{\tilde{U}}{\frac{1}{2}(\tilde{g} - \tilde{g}_c)^3} \mathrm{d}\tilde{g} + \mathrm{i}\pi \tilde{U}_{\tilde{g}\tilde{g}c} \right] \mathrm{d}\zeta. \tag{B 42}$$

Setting $h = 0$ shows that, apart from differences in notation, (B 41) reproduces the results given in GW, i.e. their (5.30) and (5.34). In the present analysis, the $\pm$ in (B 41*b*) correspond to solutions for $\hat{p}$ that are either odd or even functions of ζ depending on the particular choice for $\tilde{U}$.

Away from $\bar{\gamma} = \frac{1}{2}$, (B 40) reduces to

$$d_{-1} d_0 d_1 + O(\sigma^6) = 0. \tag{B 43}$$

The solutions to (B 43) that match onto (B 41) as $\bar{\gamma} \to \frac{1}{2}$ are

$$\left[\tilde{\alpha}_{r0}^{(I)2} + \tilde{\beta}^2 (\bar{\gamma} - 1)^2 \right]^{1/2} = \lambda_B \tilde{c}_{r0}^{(I)}, \quad \left(\cos\tilde{\theta}^{(I)} + \frac{1}{\cos\tilde{\theta}^{(I)}} \right) \tilde{\alpha}_{i0}^{(I)} = \frac{\pi \tilde{c}_{r0}^{(I)4}}{4\lambda_B}, \tag{B 44}$$

and

$$\left(\tilde{\alpha}_{r0}^{(II)2} + \tilde{\beta}^2 \bar{\gamma}^2 \right)^{1/2} = \lambda_B \tilde{c}_{r0}^{(II)}, \quad \left(\cos\tilde{\theta}^{(II)} + \frac{1}{\cos\tilde{\theta}^{(II)}} \right) \tilde{\alpha}_{i0}^{(II)} = \frac{\pi \tilde{c}_{r0}^{(II)4}}{4\lambda_B}. \tag{B 45}$$

By including the next-order corrections to (B 44) and (B 45) and then introducing (B 35), one can show that, when the minus sign is taken in (B 41*b*), (B 41) matches onto (B 44) as $h \to -\infty$ and onto (B 45) as $h \to +\infty$ or *vice versa* when the plus sign is taken in (B 41*b*). It follows that (B 41), (B 44) and (B 45) can be combined to form a set of (multiplicative) composite equations that are uniformly valid for $0 \leqslant \bar{\gamma} \leqslant \frac{1}{2}$. These equations read

$$\left[\tilde{\alpha}_{r0}^{(I)2} + \tilde{\beta}^2 (\bar{\gamma} - 1)^2 \right]^{1/2} = \lambda_B \tilde{c}_{r0}^{(I)}, \tag{B 46a}$$

$$\left(\cos\tilde{\theta}^{(I)} + \frac{1}{\cos\tilde{\theta}^{(I)}}\right)\tilde{\alpha}_{i0}^{(I)} = \frac{\pi\,\tilde{c}_{r0}^{(I)4}}{4\lambda_B}$$
$$-\frac{1}{\sigma^3}\left(\frac{\tilde{c}_{r0}^{(I)}}{\tilde{c}_{r0}}\right)^4 \mathrm{Im}\left\{[\tfrac{1}{2}\sigma^3\lambda_B^2\tilde{c}_{r0}^2\omega_1\cos 2\tilde{\theta}]^2 + [\tilde{\beta}(\bar{\gamma}-\tfrac{1}{2})\sin\tilde{\theta}]^2\right\}^{1/2}, \quad (B\,46b)$$

and

$$\left(\tilde{\alpha}_{r0}^{(II)2} + \tilde{\beta}^2\bar{\gamma}^2\right)^{1/2} = \lambda_B\tilde{c}_{r0}^{(II)}, \quad (B\,47a)$$

$$\left(\cos\tilde{\theta}^{(II)} + \frac{1}{\cos\tilde{\theta}^{(II)}}\right)\tilde{\alpha}_{i0}^{(II)} = \frac{\pi\,\tilde{c}_{r0}^{(II)4}}{4\lambda_B}$$
$$+\frac{1}{\sigma^3}\left(\frac{\tilde{c}_{r0}^{(II)}}{\tilde{c}_{r0}}\right)^4 \mathrm{Im}\left\{[\tfrac{1}{2}\sigma^3\lambda_B^2\tilde{c}_{r0}^2\omega_1\cos 2\tilde{\theta}]^2 + [\tilde{\beta}(\bar{\gamma}-\tfrac{1}{2})\sin\tilde{\theta}]^2\right\}^{1/2}, \quad (B\,47b)$$

where $\tilde{c}_{r0}$ and ω_1 are determined from (B 41a) and (B 42), respectively. The results predicted by (B 46) and (B 47) are easily extended to the range $\frac{1}{2} \leqslant \bar{\gamma} \leqslant 1$ by using the relation (5.4).

REFERENCES

BENNETT, J. & HALL, P. 1988 On the secondary instability of Taylor–Görtler vortices to Tollmien–Schlichting waves in fully developed flows. *J. Fluid Mech.* **186**, 445–469.

BRILEY, W. R. & MCDONALD, H. 1984 Three-dimensional viscous flows with large secondary velocity. *J. Fluid Mech.* **144**, 47–77.

DAVIS, R. T. & RUBIN, S. G. 1980 Non-Navier Stokes viscous flow computations. *Comput. Fluids* **8**, 101–131.

ELLINGSEN, T. & PALM, E. 1975 Stability of linear flow. *Phys. Fluids* **18**(4), 487–488.

GOLDSTEIN, M. E. & WUNDROW, D. W. 1995 Interaction of oblique instability waves with weak streamwise vortices. *J. Fluid Mech.* **284**, 377–407 (referred to herein as GW).

HALL, P. & HORSEMAN, N. J. 1991 The linear inviscid secondary instability of longitudinal vortex structures in boundary layers. *J. Fluid Mech.* **232**, 357–375.

HALL, P. & SEDDOUGUI, S. 1989 On the onset of three-dimensionality and time dependence in Görtler vortices. *J. Fluid Mech.* **204**, 405–420.

HAMILTON, J. M. & ABERNATHY, F. H. 1994 Streamwise vortices and transition to turbulence. *J. Fluid Mech.* **264**, 185–212.

HENNINGSON, D. S. 1987 Stability of parallel inviscid shear flow with mean spanwise variation. The Aeronautical Research Institute of Sweden, Aerodynamics Department. *FFA TN* 1987-57.

HUGHES, T. H. 1972 Variable mesh numerical method for solving the Orr–Sommerfeld equation. *Phys. Fluids* **15**(5), 725–728.

HULTGREN, L. S. 1992 Nonlinear spatial equilibration of an externally excited instability wave in a free shear layer. *J. Fluid Mech.* **236**, 635–664.

HULTGREN, L. S. & GUSTAVSSON, L. H. 1981 Algebraic growth of disturbances in a laminar boundary layer. *Phys. Fluids* **24**(6), 1000–1004.

LANDAHL, M. T. 1990 On sublayer streaks. *J. Fluid Mech.* **212**, 593–614.

LI, F. & MALIK, M. R. 1995 Fundamental and subharmonic secondary instabilities of Görtler vortices. *J. Fluid Mech.* **297**, 77–100.

RUBIN, S. G., KHOSLA, P. K. & SAARI, S. 1977 Laminar flow in rectangular channels. *Comput. Fluids* **5**, 151–173.

SWEARINGEN, J. D. & BLACKWELDER, R. F. 1987 The growth and breakdown of streamwise vortices in the presence of a wall. *J. Fluid Mech.* **182**, 255–290.

WUNDROW, D. W. & GOLDSTEIN, M. E. 1994 Nonlinear instability of a uni-directional transversely sheared mean flow. *NASA TM* 106779.

REPORT DOCUMENTATION PAGE

Form Approved
OMB No. 0704-0188

1. AGENCY USE ONLY (*Leave blank*)	2. REPORT DATE	3. REPORT TYPE AND DATES COVERED
	October 1996	Final Contractor Report

4. TITLE AND SUBTITLE

Linear Instability of a Uni-Directional Transversely Sheared Mean Flow

5. FUNDING NUMBERS

WU-505-90-53
C-NAS3-27186

6. AUTHOR(S)

David W. Wundrow

7. PERFORMING ORGANIZATION NAME(S) AND ADDRESS(ES)

NYMA, Inc.
2001 Aerospace Parkway
Brookpark, Ohio 44142

8. PERFORMING ORGANIZATION REPORT NUMBER

E-10458

9. SPONSORING/MONITORING AGENCY NAME(S) AND ADDRESS(ES)

National Aeronautics and Space Administration
Lewis Research Center
Cleveland, Ohio 44135-3191

10. SPONSORING/MONITORING AGENCY REPORT NUMBER

NASA CR-198535

11. SUPPLEMENTARY NOTES

Project Manager, Marvin E. Goldstein, Lewis Research Academy, NASA Lewis Research Center, organization code 0100, (216) 433-5825.

12a. DISTRIBUTION/AVAILABILITY STATEMENT

Unclassified - Unlimited
Subject Category 02

This publication is available from the NASA Center for AeroSpace Information, (301) 621-0390.

12b. DISTRIBUTION CODE

13. ABSTRACT (*Maximum 200 words*)

The effect of spanwise-periodic mean-flow distortions (i.e. streamwise-vortex structures) on the evolution of small-amplitude, single-frequency instability waves in an otherwise two-dimensional shear flow is investigated. The streamwise-vortex structures are taken to be just weak enough so that the spatially growing instability waves behave (locally) like linear perturbations about a uni-directional transversely sheared mean flow. Numerical solutions are computed and discussed for both the mean flow and the instability waves. The influence of the streamwise-vortex wavelength on the properties of the most rapidly growing instability wave is also discussed.

14. SUBJECT TERMS

Shear flow; Streamwise vorticity; Secondary instability

15. NUMBER OF PAGES

49

16. PRICE CODE

A03

17. SECURITY CLASSIFICATION OF REPORT	18. SECURITY CLASSIFICATION OF THIS PAGE	19. SECURITY CLASSIFICATION OF ABSTRACT	20. LIMITATION OF ABSTRACT
Unclassified	Unclassified	Unclassified	